



Pressure–Rate-of-Strain, Pressure Diffusion, and Velocity–Pressure-Gradient Tensor Measurements in a Cavity Flow

Xiaofeng Liu*

San Diego State University, San Diego, California 92182-1308

and

Joseph Katz†

Johns Hopkins University, Baltimore, Maryland 21218

DOI: 10.2514/1.J056168

Pressure-related turbulence statistics in a two-dimensional open cavity shear layer flow was investigated experimentally at a Reynolds number of 4.0×10^4 based on a cavity length of 38.1 mm. Time-resolved particle image velocimetry sampled at 4500 frames per second and 25×25 mm field of view was used to simultaneously measure the instantaneous velocity and pressure distributions. Direct estimate results of the pressure–rate-of-strain, pressure diffusion, and velocity–pressure-gradient tensor components based on 140,000 measurement samples were presented after a brief review of the theory about the pressure-related terms in the context of turbulence modeling and a discussion about their role in determining an accurate mean flow. The analysis is also augmented with comparisons with experimental data obtained at a higher Reynolds number of 3.4×10^5 . The pressure and streamwise velocity correlation changes its sign from negative values far upstream in the shear layer to positive ones near the trailing corner due to the strong adverse pressure gradient imposed by the corner. The distribution patterns of the pressure diffusion and the turbulence diffusion are considerably different, indicating that the conventional practice of modeling the transport terms all together as Laplacians of the turbulent kinetic energy is not justifiable, at least for the turbulent shear layer flow past a cavity. In the shear layer, turbulence fluctuation energy is redistributed from streamwise to lateral components. This intercomponent energy transfer is reversed on top of the trailing corner, indicating the complexity of the flow, especially around the corner area.

Nomenclature

C_p	=	pressure coefficient
d	=	displacement of seeding particles within the particle image velocimetry (PIV) interrogation window
L	=	cavity length
U_e	=	external freestream velocity
u	=	streamwise velocity component in the x -direction
\bar{u}	=	time-averaged streamwise velocity component
u'	=	fluctuating streamwise velocity component
v	=	lateral velocity component in the y -direction
\bar{v}	=	time-averaged lateral velocity component
v'	=	fluctuating lateral velocity component
\bar{w}	=	time-averaged spanwise velocity component
w'	=	fluctuating spanwise velocity component
\mathbf{x}_a	=	location of particle group within the PIV interrogation window
δt	=	time interval between consecutive PIV images
θ	=	momentum thickness
ρ	=	density of water

I. Introduction

TURBULENCE is a fundamental flow phenomenon widely seen in nature and engineering applications. To accurately quantify the effects caused by turbulence, adequate physics-based turbulence

modeling is needed. This is of pivotal importance to computational fluid dynamics (CFD) in particular and the simulation-based engineering science (SBES) in general. Example application areas ([1], NSF Blue Ribbon Panel report) that would be affected by physics-based turbulence modeling include, but not limited to, aerodynamic force prediction for aircraft, automobile, ship propeller, wind turbine, and jet engine designs; hazardous weather forecasting; oceanic flow influence on global climate changes; and evaluation of cardiovascular flow on human heart health.

Consistent with the NSF report, a NASA report *CFD Vision 2030 Study: A Path to Revolutionary Computational Aerosciences* [2] places exclusive emphasis on both Reynolds-averaged Navier–Stokes (RANS) and large-eddy simulation (LES) approaches as the choice of methods for computational tools to cope with grand challenges envisioned by 2030. A critical element to the process of achieving physics-based predictive modeling is high-quality experimental data at realistic high Reynolds numbers. However, lack of data, especially the experimentally obtained pressure-related terms, for example, pressure diffusion and pressure–rate-of-strain terms in the Reynolds stress transport equation, has greatly hindered the development of physics-based turbulence models. As noted by the NASA CFD Vision 2030 report, RANS turbulence models have nearly seen stagnant development for 20 years [2,3]. It is based on this observation that this paper attempts to present some recently obtained experimental data on the pressure-related statistical terms for a turbulent shear layer flow over an open cavity.

Major difficulties that result in the prolonged lack of experimental data on pressure-related turbulence statistics reside in the lack of reliable means for simultaneous measurement of instantaneous pressure and velocity distributions in flow field. In the past decade or so, efforts in developing nonintrusive pressure measurement techniques have been carried out extensively in the fluids community. It is shown that the instantaneous pressure distribution in an incompressible turbulent flow field can be reconstructed by integration of the measured material acceleration, as demonstrated by Liu and Katz [4–8], van Oudheusden [9], Ragni et al. [10], and Joshi et al. [11], to name a few. The material acceleration constitutes the dominant contributor to pressure gradient with the viscous term being

Presented as Paper 2017-1478 at the AIAA SciTech Forum 2017, Grapevine, TX, 9–13 January 2017; received 18 May 2017; revision received 17 May 2018; accepted for publication 18 May 2018; published online 14 August 2018. Copyright © 2018 by the American Institute of Aeronautics and Astronautics, Inc. All rights reserved. All requests for copying and permission to reprint should be submitted to CCC at www.copyright.com; employ the ISSN 0001-1452 (print) or 1533-385X (online) to initiate your request. See also AIAA Rights and Permissions www.aiaa.org/randp.

*Assistant Professor, Department of Aerospace Engineering; xiaofeng.liu@sdsu.edu. Associate Fellow AIAA.

†Professor, Department of Mechanical Engineering. Senior Member AIAA.

negligible for flow at high Reynolds number and away from wall, and can be measured nonintrusively using particle image velocimetry (PIV), either discretely [4–7] or continuously [8,11] time-resolved. Once the material acceleration is obtained, the pressure gradient is known. Further integrating, the pressure can be obtained. So far there are three major types of integration methods: direct line integration, Poisson equation, and least-square reconstruction that have been introduced and developed for pressure reconstruction from the measured material acceleration. For direct line integration, representative method is the so-called circular virtual boundary, omni-directional integration [4–8] over the entire measurement domain, which was evolved recently to a new algorithm featuring rotating parallel ray [12] as integration path guidance. This new “rotating parallel ray” omni-directional integration algorithm was recently successfully applied to three-dimensional (3D) pressure reconstruction based on time-resolved tomographic PIV measurement of a turbulent channel flow over compliant wall [13]. A simplified multiple-line integration approach was proposed by Dabiri et al. [14], in which the pressure was reconstructed using median polling of the integration results along several integration paths originated from typically eight surrounding directions. However, as demonstrated by Wang et al. [15], the eight-path integration of Dabiri et al. [14] suffers from a considerable compromise in pressure reconstruction accuracy in comparison with Liu and Katz’s omni-directional approach, although the amount of computation of the former is significantly reduced when compared with the latter. Representative Poisson equation approach can be found in de Kat and van Oudheusden [16,17], Violato et al. [18], and Auteri et al. [19]. Review and comparison of the direct line integration and Poisson equation pressure reconstruction approaches can be found in Charonko et al. [20] and van Oudheusden [21]. The robustness of the omni-directional integration method has been confirmed by Charonko et al. [20]. The least-square reconstruction approach [22] was recently used to experimentally obtain instantaneous pressure field in a wake of a separated flow over an airfoil. This approach was also referred to as direct matrix inversion by Liu and Katz [5]. Actually, as demonstrated by Wang et al. [23], the least-square approach is mathematically equivalent to the Poisson equation approach with Neumann boundary conditions.

In addition to the above integration approaches, recently several new methods were introduced for pressure reconstruction. For example, with time-resolved 3D3C velocity field data available, Tronchin et al. [24] demonstrated the feasibility of using a conventional CFD pressure reconstruction approach to iteratively solve the discretized Eulerian-based Navier–Stokes equation over a “chimera mesh,” treating the pressure as an unknown quantity and the measured velocity components as known ones. Using a Poisson solver, Neeteson and Rival [25] proposed a Lagrangian finite-volume method to obtain pressure values at particle positions determined by the Shake The Box (STB) algorithm [26]. In contrast to the conventional Poisson approach, Huhn et al. [27] introduced a method of 3D pressure field reconstruction in the Fourier space using a Fast Fourier Transform (FFT) method. Exploiting the curl-free property of the pressure gradient as a constraint, Wang et al. [15] developed a proper orthogonal decomposition (POD)–based pressure reconstruction approach, with the curl-free constrained POD as an error reduction treatment and the simple cross-line integration as the final step for obtaining the pressure. Most recently, van Gent et al. [28], using a simulated experiment from a zonal detached eddy simulation of an axisymmetric base flow at Mach 0.7, conducted a massive comparison study for pressure reconstruction methods, including the Poisson solver [17], least-square [22], FFT [27], Taylor’s hypothesis and Poisson solver [29], and Voronoi–Lagrangian finite-volume–based Poisson solver [25], and concluded that, although with different degrees of accuracy in reconstructed pressure distributions, all methods were able to capture the main features of the instantaneous pressure fields, including the method of de Kat and Ganapathisubramani [29], which reconstructs the pressure from a single PIV velocity snapshot based on Taylor’s hypothesis for acceleration estimate.

The aforementioned efforts in PIV-based pressure measurement tool development provide the possibility of measuring much-needed pressure-related statistics in turbulent flows. In particular, this paper reports the results of the planar pressure diffusion and pressure–strain terms measured in a cavity shear layer flow at a Reynolds number of

40,000 based on the cavity length, using the virtual boundary omni-directional pressure reconstruction method. We need to recognize that before the results presented in this paper, there have been plenty of numerical based data on pressure-related turbulence statistics, obtained either using direct numerical simulation (DNS) (e.g., [30–32]), or LES (e.g., [33]). Also there have been attempts to measure the planar pressure diffusion and/or pressure–rate-of-strain terms either directly or indirectly before. For example, Kawata and Obi [34] measured pressure-related statistics for a cylinder wake flow at a diameter-based Reynolds number of 7800 by reconstructing the POD modes of pressure with a two-dimensional (2D) Poisson equation. Liu and Thomas [35], Gutmark and Wignanski [36], and Wignanski and Fiedler [37] obtained pressure diffusion estimates by balancing all other terms in turbulence kinetic energy transport equation. As for point pressure–velocity correlation measurement, representative efforts using combination of pressure and X-wire probes include those of Kawata et al. [38] in a near wake flow, Terashima et al. [39] in a planar jet, Naka and Obi [40] in free shear flows, and Naka et al. [41] in a mixing layer. It is worth mentioning that as an earlier effort using a four-hole cobra probe, Hooper and Musgrove [42] conducted point pressure–velocity correlation measurement in a turbulent pipe flow.

The organization of this paper is as follows. Section II briefly reviews the theory about the pressure-related turbulence transport terms. Section III presents the experimental setup. Section IV describes the material acceleration and the nonintrusive pressure measurement techniques used in the experiment. The measurement results are shown in Sec. V, which is followed by discussion and conclusion in Sec. VI.

II. Theory About Pressure-Related Turbulence Terms

As summarized by Pope [43], RANS turbulence models can be classified into two major classes: the turbulent-viscosity models and the Reynolds-stress and related models. The turbulent-viscosity models, listed in order of increasing level of description, include mixing length (e.g., [44,45]), one-equation ν_T (e.g., [46–48]), one-equation $k - l_m$ (i.e., Prandtl’s one-equation model), two-equation $k - \epsilon$ (e.g., [49,50]), and two-equation $k - \omega$ (e.g., [51,52]) models. Compared with the turbulent-viscosity models, the Reynolds-stress models do not require turbulent-viscosity hypothesis, thus eliminating one of the major defects of the turbulent-viscosity models. In Reynolds-stress models, individual Reynolds stresses are solved from the following transport equation:

$$\begin{aligned} \frac{D}{Dt} (\overline{u'_i u'_j}) &= - \frac{\partial}{\partial x_k} \overline{u'_i u'_j u'_k} \\ \text{Material derivative of Reynolds stress (unsteady+convection terms)} & \quad \text{Turbulence diffusion} \\ + \frac{\partial}{\partial x_k} \left(\nu \frac{\partial}{\partial x_k} \overline{u'_i u'_j} \right) &+ \underbrace{P_{ij}}_{\text{Production}} + \underbrace{\Pi_{ij}}_{\text{Velocity-pressure-gradient}} - \underbrace{\epsilon_{ij}}_{\text{Dissipation}} \end{aligned} \quad (1)$$

where the velocity–pressure-gradient tensor

$$\Pi_{ij} = - \frac{1}{\rho} \overline{\left(u'_i \frac{\partial p'}{\partial x_j} + u'_j \frac{\partial p'}{\partial x_i} \right)} \quad (2)$$

can be further decomposed into pressure diffusion

$$- \frac{\partial T_{kij}^p}{\partial x_k} = - \frac{1}{\rho} \left(\overline{\frac{\partial u'_j p'}{\partial x_i}} + \overline{\frac{\partial u'_i p'}{\partial x_j}} \right) \quad (3)$$

and pressure–rate-of-strain tensors,

$$R_{ij} = \frac{p'}{\rho} \left(\frac{\partial u'_i}{\partial x_j} + \frac{\partial u'_j}{\partial x_i} \right) \quad (4)$$

that is,

$$\Pi_{ij} = R_{ij} - \frac{\partial T_{kij}^p}{\partial x_k} \quad (5)$$

Please note that the above decomposition of the velocity–pressure-gradient tensor is not unique. The decomposition is intended to facilitate turbulence modeling, as describe by Pope [43]. The velocity–pressure-gradient tensor and the associated decomposition are critical for understanding and modeling turbulence [43,53,54]. In the process of turbulence kinetic energy (TKE) transport, the pressure diffusion represents the mechanism due to pressure fluctuation for the redistribution of TKE from places where the energy is newly generated, to places where there is a lack of the new TKE, so as to help the turbulence field to become more homogeneous [35]. In contrast, the pressure–rate-of-strain terms, as indicated by the equation

$$R_{11} + R_{22} + R_{33} = 0 \quad (6)$$

are responsible for redistribution of energy among components of the turbulence normal stresses, that is, intercomponent energy transfer among fluctuating components. This intercomponent energy transfer serves as the primary mechanism for the return-to-isotropy process [43] of the anisotropic turbulence commonly seen in turbulent shear flows, thus playing a major role in defining turbulence development. Two equation models like $k - \epsilon$ make no attempt to differentiate between the three fluctuating velocity components. Indeed if the transport equations for components of Reynolds normal stresses $\overline{u'^2}$, $\overline{v'^2}$, and $\overline{w'^2}$ are summed, pressure–rate-of-strain terms disappear altogether and so do not appear in the turbulent kinetic energy transport equation.

In the popular eddy viscosity models of the RANS simulation approach, a common practice is to combine the transport terms and model them as [43,55–58]:

$$\frac{1}{\rho} \overline{p'u'} + \frac{1}{2} \overline{u'_i u'_j u'_j} - 2\nu \overline{u'_j s'_{ij}} = -\frac{\nu_T}{\sigma_k} \nabla k \quad (7)$$

where σ_k is usually taken as 1, based on the assumption that pressure diffusion follows the same pattern as that of the turbulence diffusion. However, there is no physical justification for this assumption. The situation becomes even more complicated if one wants to use a better Reynolds stress model and solve approximated evolution equations for Reynolds stresses. Modeling R_{ij} or Π_{ij} has been a major obstacle, in substantial part due to lack of pressure data, which hinders the understanding of the correct relationship between these pressure terms and other relevant ones such as the production and the Reynolds stress terms. As a result, even arguments about validity of models are based on postulated theoretical arguments, for example, asymptotic conditions (rapid distortion theory) as opposed to direct comparisons to measured pressure–strain terms.

Traditionally, the pressure–rate-of-strain term has been decomposed to rapid, slow, and harmonic parts, and numerous models have been introduced [43,59]. For example, the popular LRR-IP model combines both slow and rapid terms [60,61]:

$$R_{ij} = -C_R \frac{\epsilon}{k} \left(\overline{u'_i u'_j} - \frac{2}{3} k \delta_{ij} \right) - C_2 \left(P_{ij} - \frac{2}{3} P \delta_{ij} \right) \quad (8)$$

Comparisons of the above relationship with DNS data of Rogers and Moin [62] show reasonable agreement in some terms and substantial discrepancy in others even for a planar shear flow at low Reynolds numbers [43]. There is no universally accepted model for the pressure-related terms [63,64], and all models have substantial fundamental deficiencies. This understanding is further confirmed through the NASA 2004 Computational Fluid Dynamics Validation Workshop on Synthetic Jets and Turbulent Separation Control (CFDVAL2004) and its subsequent validation efforts (e.g., [33,65]). In particular, for Case 3 of the CFDVAL2004 workshop, which investigates a turbulent flow over a wall-mounted hump (NASA hump) with a Glauert-Goldschmied-type airfoil shape contour reveals, the turbulent boundary-layer separation imposes great challenges to

simulation, as evident from the underpredicted turbulent shear stresses in magnitude inside the separation bubble, and the correspondingly overpredicted size of the mean separation bubble that leads to a delayed predicted reattachment. A recent investigation of the hump flow [59] further indicates that the near-wall inhomogeneity causes pressure–rate-of-strain models to predict incorrect signs for the normal pressure–strain components close to the wall. These examples demonstrate how important it is to accurately characterize the behavior of the pressure-related terms in order to accurately determine the mean flow.

To obtain a better understanding of the complex relationships among the turbulence quantities, especially the pressure-related terms, in this paper we present pressure-related turbulence statistics in a 2D open cavity shear layer flow, with a focus on the flow field around the shear layer impingement point on the trailing corner of the cavity. These data can be used for calibration and improvement of the turbulence models such as Eqs. (7) and (8).

III. Experimental Setup

The experiment has been conducted in a small water tunnel described by Gopalan and Katz [66] and Liu and Katz [5]. Details about the experimental setup can be found by Liu and Katz [8] (hereinafter referred to as LK13) as well as Liu and Katz [6] (hereinafter referred to as LK07). To present the new information on the pressure-related statistics, only essential features about the setup are repeated here. As sketched in Fig. 1, a 38.1-mm-long, 50.8-mm-wide, and 30.0-mm-deep 2D cavity model is constructed of a transparent acrylic insert that is installed in the 50.8 mm (width) \times 63.5 mm (height) test section. Thus the tunnel height (63.5 mm) versus the step and cavity height (30.0 mm) is 2.12 : 1. A 13-mm-long region with tripping grooves, each with a notch depth of 0.46 mm and width of 1.00 mm, is machined at the beginning of the bottom wall of the test section in order to trip the boundary layer. Thus, the separating boundary layer at the beginning of the cavity is turbulent. For most of the experiments described in this paper, the mean velocity above the cavity is $U_\infty = 1.20$ m/s, corresponding to a Reynolds number of 4.0×10^4 based on cavity length. The mean pressure in the

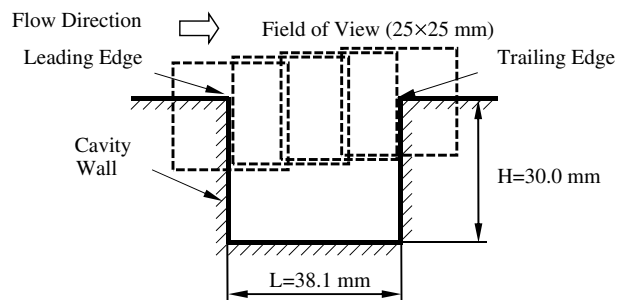
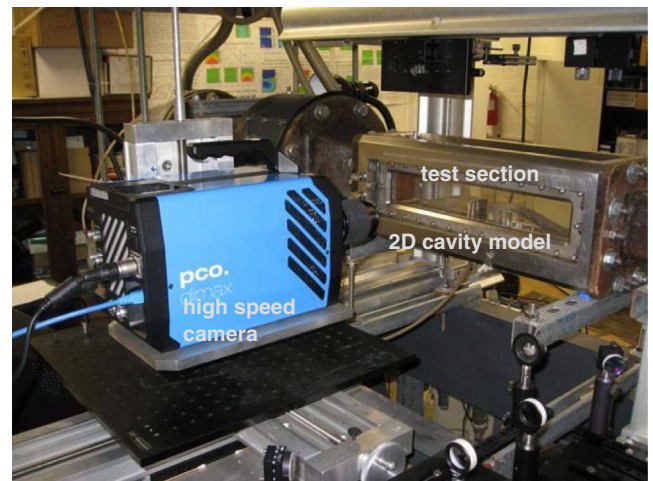


Fig. 1 Experimental setup and cavity geometry.

water-tunnel facility is well above the conditions that would cause occurrence of cavitation during the PIV measurements. The streamwise length of the cavity normalized by the momentum thickness of the boundary layer at the leading edge of the cavity, L/θ_0 , is 127, sufficiently large for self-sustained shear layer oscillation. Based on Gharib [67] and Gharib and Roshko [68], the minimum L/θ_0 for such oscillation is about 80. The origin of the coordinate system used in this paper is placed at the leading edge of the cavity, with the x and y axes pointing downstream and upward, respectively. The instantaneous, ensemble averaged, and fluctuating horizontal and vertical velocity components are denoted as u , v , \bar{u} , \bar{v} , u' , and v' , respectively.

To perform time-resolved, 2D PIV measurements, we use a Photonics DM60-527 Nd:YLF laser that has a maximum pulse rate of 10 kHz, and pulse width of 100 ns. The images are recorded at 4500 frames per second using a PCO.dimax CMOS camera, at a resolution of 1008×1000 pixels, giving a Nyquist frequency of 2250 Hz for the velocity and 563 Hz for the material acceleration and pressure (see Sec. IV for explanation). To synchronize the laser with the camera, we use a Quantum Composer model 9618 pulse generator. The selected temporal resolution is sufficient for resolving the Kolmogorov time scale, found to be $673 \mu\text{s}$, based on curve fits to the spatial energy spectra for the dissipation rate estimate. The size of the field of view is 25×25 mm to maintain sufficient resolution, requiring us to record data in multiple adjacent sample areas, all aligned with the central plane of the cavity setup. With an appropriate concentration of seed particles, 8–12- μm -diam hollow glass spheres with specific gravity of 1.05–1.15, we are able to use an interrogation window size of 16×16 pixels, corresponding to 0.4×0.4 mm. This size is similar to the estimated Taylor transverse microscale of 0.5 mm, but is an order of magnitude larger than the Kolmogorov length scale of $26 \mu\text{m}$. A 50% overlap between the interrogation windows gives a vector spacing of 0.2 mm. We use in-house developed software [69,70] for calculating the velocity. A total of four sample areas with the same field-of-view size, but shifted horizontally with 50% overlap, are used to cover the flow field, from the boundary layer upstream of the leading corner to the flow over the trailing corner. The present analysis focuses on the field of view that covers the cavity trailing corner, where we have processed and analyzed 14 statistically independent datasets, with each set being acquired separately in time with sufficiently long time intervals. Each set consists of 10,000 sequentially obtained instantaneous realizations over a period of 2.22 s (i.e., about 3.8 flapping cycles of the slowest characteristic unsteady motion of the shear layer). Thus a total of 140,000 instantaneous realizations over a collectively 31 s of sampling time accumulated from the 14 statistically independent sampling segments have been analyzed. These datasets cover a total of 53 flapping cycles for the trailing corner measurement station, which turns to be sufficient to ensure the convergence of the associated ensemble-averaged statistics (will be discussed in details in Sec. V.F).

We have also used velocity distributions obtained previously at a higher Reynolds number (3.4×10^5 [4–7]) using a larger format camera, at the same spatial resolution (interrogation window of 0.4×0.4 mm), but at a much lower sampling frequency (2 Hz). In those measurements, the data consist of ensembles of 860 realizations that are not continuously time-resolved. The field of view is 50.8×50.8 mm covering the entire cavity, the vector spacing is 0.2 mm, and the free stream velocity is 10 m/s. The pressure-related terms for this large field-of-view experiment (Reynolds number 3.4×10^5) will also be presented as a comparison to those obtained from the aforementioned detailed small field of experiment (Reynolds number of 4.0×10^4).

For all these experiments, the planar PIV measurements were conducted at the central span of the cavity flow field, where the flow field is 2D in the mean, and the instantaneous 3D effect is expected to be minimal compared with other planes in the spanwise direction.

IV. Analysis Procedures

The procedures for obtaining the velocity and the material acceleration, though still following the principle described by

Liu and Katz [5], have been modified to take advantage of the time resolved data series. Analysis of each pair of consecutive images provides an instantaneous velocity distribution, and the entire set provides a time series $\mathbf{u}_1, \mathbf{u}_2, \mathbf{u}_3, \dots, \mathbf{u}_M$, where M denotes the final sequential number for the velocity time series in a data set. Five consecutive images are used for calculating the acceleration. To calculate the velocity field at time t_i , we use

$$\mathbf{u}_i(\mathbf{x}_a, t_i) = \frac{\mathbf{d}_{i,i+1}(\mathbf{x}_a, t_i) - \mathbf{d}_{i,i-1}(\mathbf{x}_a, t_i)}{2\delta t} \quad (9)$$

where $\mathbf{d}_{i,i+1}$ is the displacement of particles obtained from cross-correlating the interrogation window in image i with that in image $i+1$. Thus, $\mathbf{u}_i(\mathbf{x}_a, t_i)$ is based on an average of $\mathbf{d}_{i,i+1}$ and $-\mathbf{d}_{i,i-1}$ of a group of particles located at \mathbf{x}_a at time t_i . We stagger our image pairs to ensure that the same particle groups are followed within the thickness of the laser sheet, an inherent requirement to obtain reliable material acceleration. The in-plane projection of material acceleration is calculated using

$$\frac{D\mathbf{u}_i}{Dt}(\mathbf{x}_a, t_i) \approx \frac{\mathbf{u}_{i+1}(\mathbf{x}_a + \mathbf{d}_{i,i+1}, t_{i+1}) - \mathbf{u}_{i-1}(\mathbf{x}_a + \mathbf{d}_{i,i-1}, t_{i-1})}{2\delta t} \quad (10)$$

This approach estimates the material acceleration components from the difference between the velocity of the same group of particles at t_{i+1} and t_{i-1} as long as the majority of the particles remains within the light sheet. It is based on the assumption that the particles are displaced by the local velocity. Based on Eqs. (9) and (10), a total of five consecutive images ($i-2, i-1, i, i+1, i+2$) are involved in the determination of the material acceleration, and subsequently, the pressure distribution. Thus the temporal resolution of the material acceleration and the pressure measurement is $888.9 \mu\text{s}$ ($4\delta t$), giving rise to a corresponding Nyquist frequency of 563 Hz. Because the displacements involve fraction of the vector spacing, calculation of the acceleration involves bi-cubic interpolation.

The instantaneous pressure distribution is obtained by integrating the measured in-plane component of the material acceleration using circular virtual boundary omni-directional integration. For high-Reynolds-number flows away from the wall, the material acceleration is much larger in magnitude than the viscous terms, as confirmed by direct calculations, and is balanced by the pressure gradients. The kernel of the pressure reconstruction procedure is the omni-directional integration. By summing up the errors embedded in the measured pressure gradients from all directions, the omni-integration minimizes the influence of the errors propagated to the final pressure result, so as to achieve a reliable and accurate pressure measurement. A history about the evolution of the omni-directional integration algorithm can be found in Liu et al. [12].

V. Measurement Results on Pressure-Related Turbulence Statistics

Unless otherwise specified, data presented and analyzed in this paper are primarily focused on and refer to those obtained in the detailed small field of view experiment with Reynolds number of 4.0×10^4 . However, whenever necessary, data obtained from the large field of view experiment with Reynolds number 3.4×10^5 will also be presented for comparison and completeness of the analysis.

A. Mean Flow Fields and Reynolds Stress Distributions

Details about the time-averaged flow features are discussed in LK13. To facilitate the analysis of the pressure-related turbulence terms, the time-averaged velocity, pressure, and vorticity distributions around the leading and trailing corners of the cavity are presented in Fig. 2 (adapted from LK13 with permission). Corresponding distributions of in-plane normal and shear Reynolds stress components as well as RMS values of pressure fluctuations are reprinted in Fig. 3 (again adapted from LK13). As shown in Fig. 2f, when the shear layer approaches the downstream corner, it is subjected to an adverse pressure gradient in the vicinity of the trailing corner, and therefore

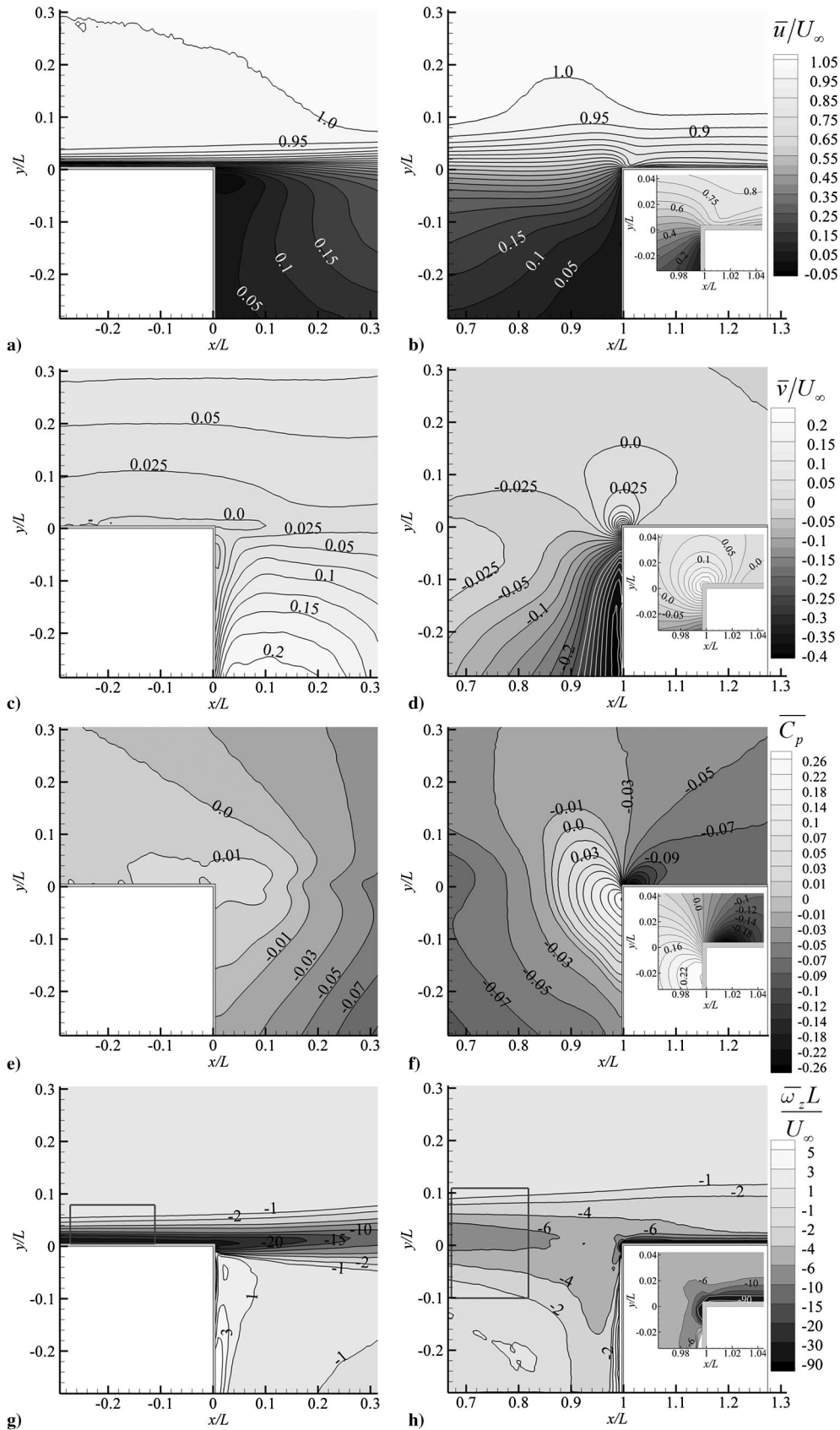


Fig. 2 Distributions of ensemble averaged (a, b) horizontal velocity, (c, d) vertical velocity, (e, f) pressure, and (g, h) spanwise vorticity around the leading (a, c, e, g) and trailing (b, d, f, h) corners of the 2D cavity. Note that the contour lines represent constant increments in (a–d), and varying increments in (e–h). (Adapted from Fig. 4 of Liu and Katz [8]. Reprint with permission from Cambridge University Press.)

decelerates, forming a mean stagnation point 1 mm ($0.026L$) below the trailing corner. After impingement on the corner, the shear layer separates with one part climbing around the corner, and the other

entrained into the cavity along the vertical wall. When the flow accelerates around the corner, it creates a pressure minimum on top of it, at about $0.013L$ downstream from the tip. Although the mean

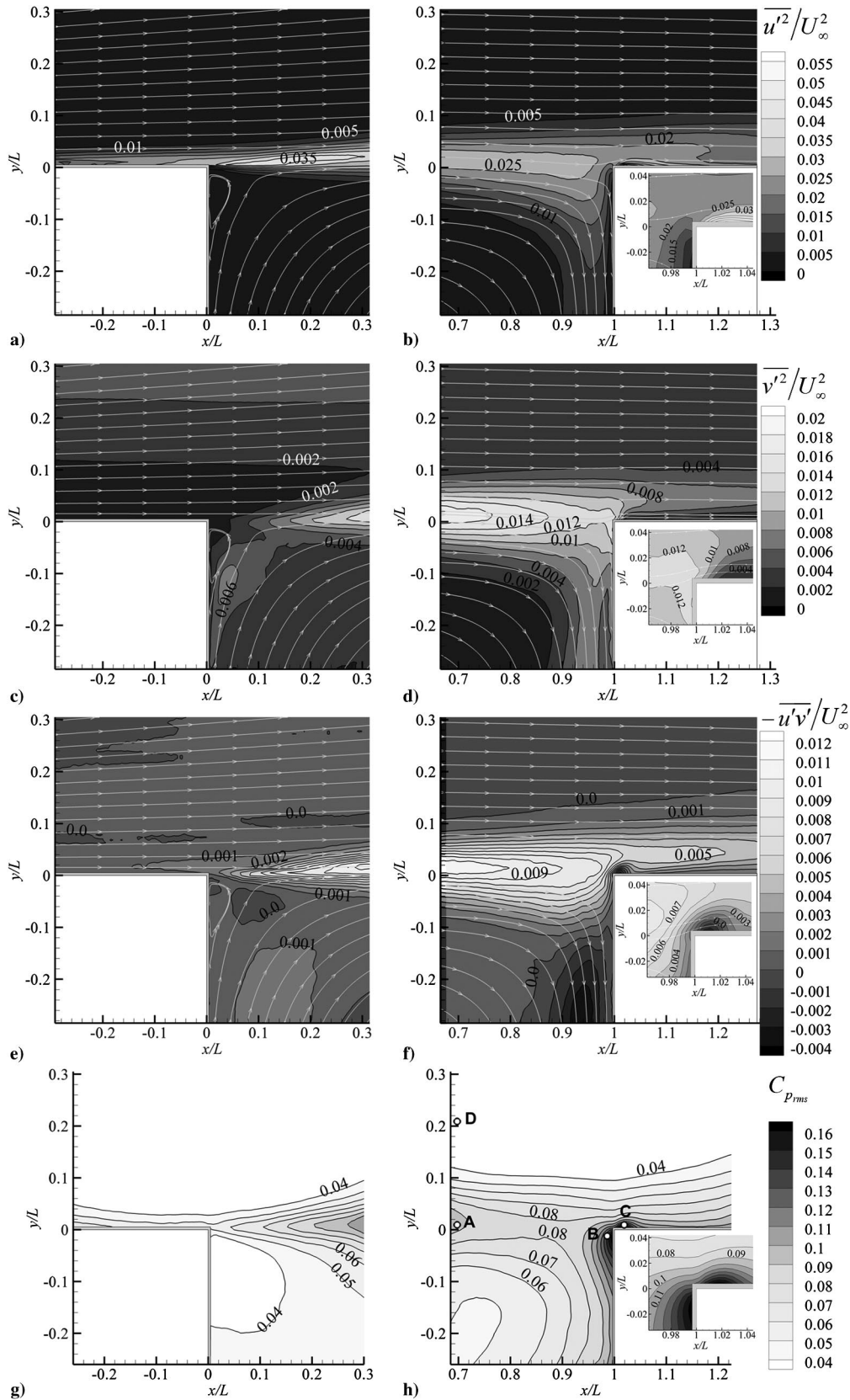


Fig. 3 Distributions of (a, b) streamwise normal stress, (c, d) lateral normal stress, (e, f) Reynolds shear stress, and (g, h) rms values of pressure fluctuation around the leading (a, c, e, g) and trailing (b, d, f, h) corners of the 2D cavity. (Adapted from Fig. 5 of Liu and Katz [8]. Reprint with permission from Cambridge University Press.)

velocity remains positive above the corner, at least at the scale of the PIV interrogation windows, examination of the particle traces shows that reverse flow occurs intermittently above the wall at scales that are below about 0.1 mm, that is, a small fraction of the window size.

The mean vorticity distributions (Figs. 2g and 2h) show the expansion of the shear layer across the cavity, which involves a six times decrease in magnitude of vorticity, and formation of a negative vorticity peak on top of the trailing corner, mainly due to

pressure-gradient-induced local vorticity production (LK13) there. Layers of positive vorticity form along the walls inside the cavity and some of this positive vorticity is entrained into the beginning of the shear layer.

The largest streamwise normal stress $\overline{u'^2}$ (Fig. 3b), with values that are roughly 60% higher than those in the shear layer, occur on top of the trailing corner. The highest $\overline{v'^2}$ (Fig. 3d) is measured in the shear layer, with peak values that are roughly one half of the streamwise component. The turbulence level along with the shear stress decays as remnants of the shear layer split and are transported above the trailing corner and into the cavity. As expected, along both walls, the velocity fluctuations in the wall-normal direction are lower than the wall-parallel one. One noteworthy phenomenon is the change in Reynolds shear stress sign just above the tip of the corner (Fig. 3f). It is caused by high negative production rate of the Reynolds shear stress there due to the large negative values of $u'^2 \partial \bar{V} / \partial x$ that occur as the wall-normal velocity decays rapidly around the corner.

B. Pressure-Velocity Correlation

As shown in Eq. (3), the pressure diffusion term involves the pressure-velocity correlation. Thus to investigate the behavior of the pressure diffusion, distributions of pressure-velocity correlation, including $\overline{p'u'}$ and $\overline{p'v'}$, are examined and shown in Fig. 4 for the experiment with small field of view (Reynolds number of 4.0×10^4) and Fig. 5 for the experiment with large field of view (Reynolds number of 3.4×10^5). To further verify the observed variations of the pressure-velocity correlation in the shear layer and around the cavity trailing corner, we compare the probability density function (PDF) profiles for the experiment with small field of view (Reynolds number of 4.0×10^4) in Fig. 6 for both $p' - u'$ and $p' - v'$ correlations at three representative locations, which are indicated in Fig. 3h. Point A ($x/L = 0.70, y/L = 0.01$) is located in the shear layer upstream of the trailing corner, and is used as a reference for the “undisturbed shear layer”; point B ($x/L = 0.99, y/L = -0.01$) is located in the high-pressure region just upstream of the corner; and

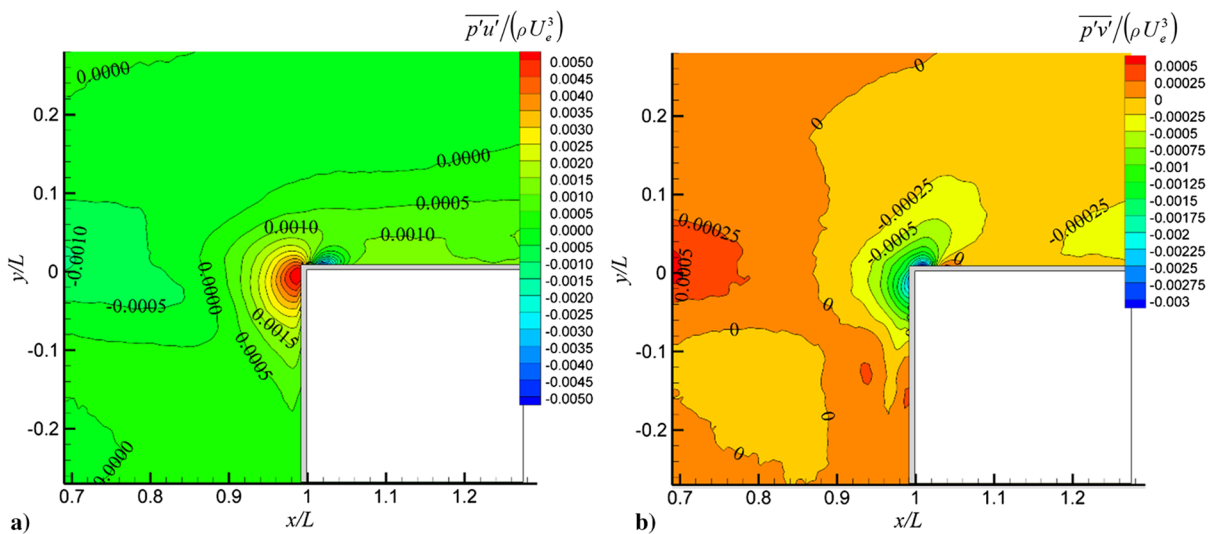


Fig. 4 Distribution of pressure-velocity correlations obtained at Reynolds number of 4.0×10^4 : a) correlation between the pressure and the streamwise velocity component $\overline{p'u'}$; b) correlation between the pressure and the lateral velocity component $\overline{p'v'}$.

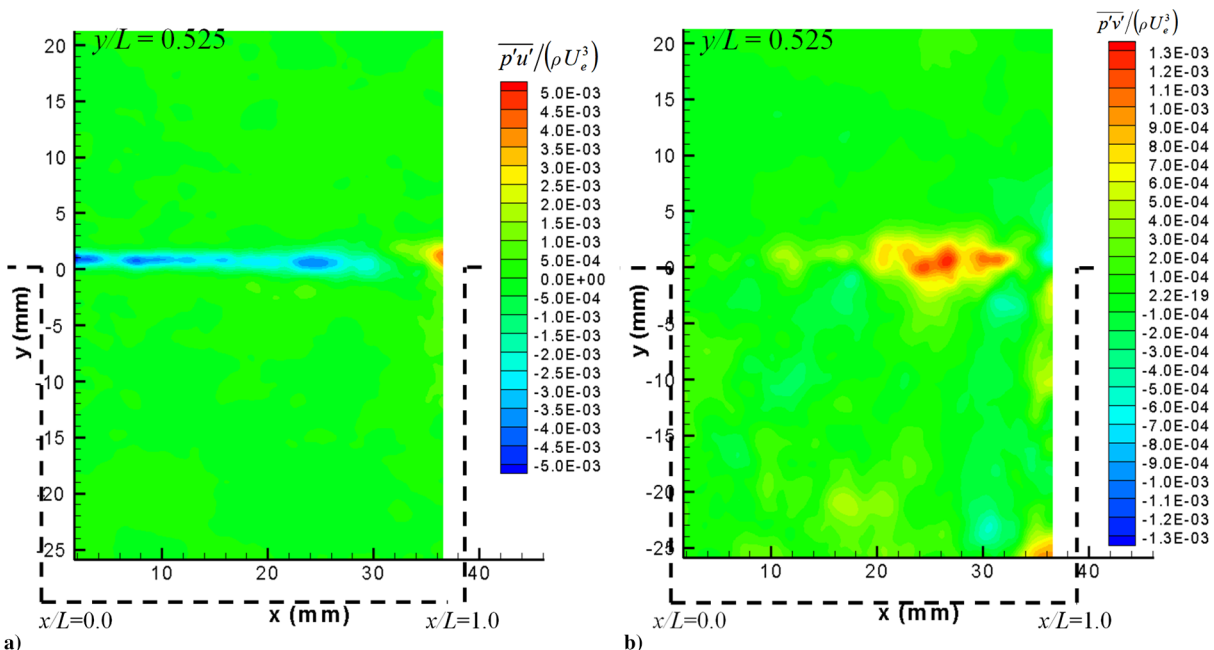


Fig. 5 Distribution of pressure-velocity correlations obtained at Reynolds number of 3.4×10^5 : a) correlation between the pressure and the streamwise velocity component $\overline{p'u'}$; b) correlation between the pressure and the lateral velocity component $\overline{p'v'}$.

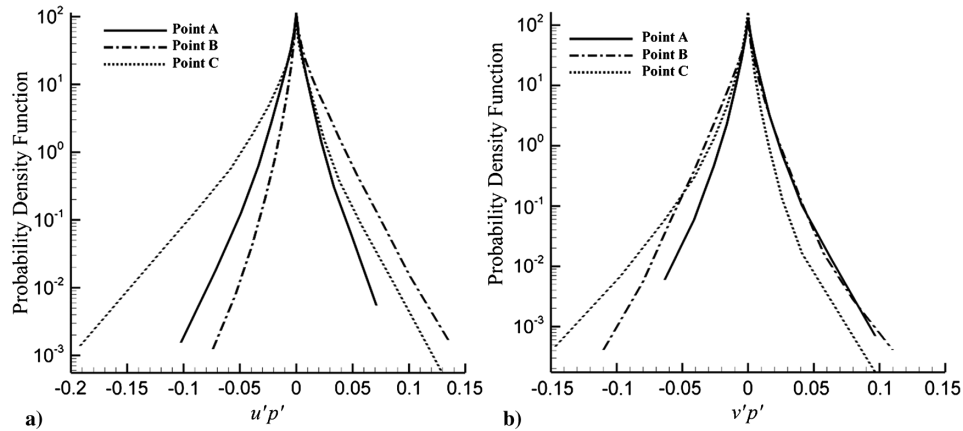


Fig. 6 Comparison of probability density function profiles of a) correlation between the pressure and the streamwise velocity component $p'u'$ and b) correlation between the pressure and the lateral velocity component $p'v'$ for points A, B, and C indicated in Fig. 3h.

point C ($x/L = 1.016$, $y/L = 0.01$) is located within the previously discussed pressure minimum region on top of the corner. Characteristics of these pdf profiles shown in Fig. 6 are summarized in Table 1.

As can be seen in Figs. 4a and 5a, in most of the shear layer, u' and p' are negatively correlated. Correspondingly we see a negatively skewed $p' - u'$ profile at location A in Fig. 6a. This negative correlation implies that the pressure decreases as the instantaneous flow locally accelerates in the streamwise direction, and vice versa, that is, an inertial “Bernoulli type” relation. Hooper and Musgrove [42], using a cobra (4-hole) probe, also report strong negative correlations between fluctuating pressure and streamwise velocity component in a developed pipe flow.

However, when the flow approaches the trailing edge of the cavity as shown in Figs. 4a and 5a, due to the presence of the adverse pressure gradient, the negative correlation of $\overline{p'u'}$ gradually decreases in magnitude and eventually changes its sign, creating a positive peak just upstream of the trailing corner. This trend is associated with the adverse mean pressure gradients and stagnation-like conditions near the cavity trailing corner (see Fig. 2f). As the momentum increases in the impinging shear layer (thus resulting a positive velocity fluctuation locally), the local adverse pressure gradient also increases (thus resulting a positive pressure fluctuation locally). Consequently, the pressure–velocity correlation $\overline{p'u'}$ becomes positive. Correspondingly, a highly positively skewed $p' - u'$ profile at location B can be found in Fig. 6a.

As for the $p'v'$ correlation shown in Figs. 4b and 5b, p' and v' are positively correlated in most of the shear layer. To explain this trend, it is sufficient to note that essentially in all shear flows u' and v' are inherently negatively correlated. A downward flow, that is, negative v' , brings high-momentum fluid to the shear layer, that is, a positive u' . However, since u' and p' are negatively correlated, p' is negative. Therefore, in this situation, p' and v' are positively correlated in the shear layer. As the shear layer approaches the trailing corner, this p' and v' correlation also changes sign in front of the trailing corner due to adverse pressure gradient. However, unlike the situation of $\overline{p'u'}$ shown in Fig. 4a, $\overline{p'v'}$ continuously maintains its negative correlation value in the area surrounding the trailing corner, as shown in Fig. 4b. These trends are consistent with the $p' - v'$ profiles shown in Fig. 6b.

The negative correlation values of $\overline{p'u'}$ and $\overline{p'v'}$ above the cavity trailing corner (Fig. 4) can be comprehended by examining the velocity and pressure distributions around cavity trailing corner as shown in Figs. 2b, 2d, and 2f. On average, when a fluid particle passes over the trailing corner, it is subjected to a favorable pressure gradient. When the favorable pressure gradient is intensified, a positive u' and a positive v' , together with a negative p' , would be found above the trailing corner. Conversely, when the favorable pressure gradient is attenuated, negative u' and v' values as well as a positive p' would occur on top of the trailing corner, thus causing a negative correlation value of $\overline{p'u'}$ and $\overline{p'v'}$ there.

The overall trend shown in Fig. 6 and Table 1 in terms of the mean statistical values $\overline{p'u'}$ and $\overline{p'v'}$ are consistent with the previous discussions about Figs. 4 and 5. In addition, as shown in Fig. 6, there are two major features associated with the pressure–velocity PDF profiles at these representative locations. First, no matter whether the point is located in the shear layer or around the trailing corner, the peaks of these PDF profiles are all located at the zero correlation value location, which means that for the majority of time in the shear layer and around the corner, pressure and velocity are not correlated. Second, the profile shapes are all asymmetric with respect to the zero correlation value location, thus giving rise to nonzero skewness values for these PDF profiles. Because the peaks of the PDF profiles are locked around zero, it is the shape asymmetry or skewed distribution that determines the final mean values of the pressure–velocity correlation. In other words, it is the less-frequent flow events that alter the shape (in terms of skewness) of the PDF profiles and subsequently determine the mean value of the pressure–velocity correlation. As a matter of fact, examination of Table 1 (which is consistent with Fig. 6) shows that the negative skewness values of $p' - u'$ PDF profiles at points A and C correspond to negative mean values of $p' - u'$ at these locations, whereas a positive skewness value of $p' - u'$ at point B corresponds to positive mean values of $p' - u'$ at that location. Similar relationship between the skewness and mean correlation value exists for the $p' - v'$ correlations shown in Table 1. Moreover, it seems that the skewness is monotonically associated with the mean pressure–velocity correlation values; that is, large magnitude of skewness values are associated with large magnitude of mean values of the pressure–velocity correlation, and vice versa.

Table 1 Statistics about pressure–velocity correlations at representative locations indicated in Fig. 3h

Location	$\overline{p'u'}/(\rho U_c^3)$				$\overline{p'v'}/(\rho U_c^3)$			
	Mean	Standard deviation	Skewness	Kurtosis	Mean	Standard deviation	Skewness	Kurtosis
A	-1.1×10^{-3}	9.0×10^{-3}	-0.60	10.6	5.5×10^{-4}	6.9×10^{-3}	0.45	13.0
B	5.2×10^{-3}	11.5×10^{-3}	2.08	11.7	-2.0×10^{-3}	9.3×10^{-3}	-0.64	9.7
C	-4.1×10^{-3}	16.0×10^{-3}	-1.84	14.0	-2.2×10^{-3}	7.4×10^{-3}	-3.01	27.2

Another quantity describing the characteristic shape of the PDF profiles is kurtosis. As shown in Table 1, the PDF profiles for both $p' - u'$ and $p' - v'$ correlations at the representative locations all have extremely high kurtosis values of $\sim \mathcal{O}(1000\sigma)$, with σ being the standard deviation of the corresponding pressure-velocity correlation distribution. These high kurtosis values indicate that the PDF profile shapes strongly deviate from that of the Gaussian distribution, for which the kurtosis value is only 3σ . Also these extremely high kurtosis values can be viewed as an evidence that shows the less-frequent flow events play an important role in determining the mean values of the pressure-velocity correlations.

C. Triple Velocity Correlation Distribution

To facilitate the subsequent discussion in Sec. V.D about pressure diffusion and turbulence diffusion, distributions of triple velocity correlations u'^3 , u'^2v' , $u'v'^2$, and v'^3 are shown in Figs. 7a–7d, respectively. As shown in Eq. (1), these triple velocity correlations are the basis for the calculation of the turbulence diffusion terms. One striking feature for the plots shown in Fig. 7 is that the distribution patterns of u'^3 and $u'v'^2$ are very similar in shape, yet with different magnitude at corresponding locations (Figs. 7a and 7c). Same type of similarity exists for the distribution patterns of u'^2v' and v'^3 (Figs. 7b and 7d) as well. These similarities in distribution pattern can be comprehended by looking into the role that u' and v' play in these triple correlation terms. Actually, u'^3 and $u'v'^2$ can be viewed as the turbulence transport (i.e., turbulence diffusion) of the Reynolds

normal stresses u'^2 and v'^2 by the u' -component fluctuation u' . Since u'^2 and v'^2 distributions as shown in Figs. 3a–3d are very similar in most part of the shear layer flow over the cavity, the transport (diffusion) of u'^2 and v'^2 by the same u' fluctuation mechanism must be also very similar. For the same reason, since the triple correlation terms u'^2v' and v'^3 represent the transport of u'^2 and v'^2 by the same v' fluctuation, the distribution patterns of these two triple correlation terms also appear to be similar.

Another feature for the triple velocity correlation distributions is that the values in the upper strips of the u'^2v' and v'^3 distributions are positive, whereas their lower parts are negative (Figs. 7b and 7d). As a contrast, reversed patterns can be found for u'^3 and $u'v'^2$ distributions (Figs. 7a and 7c). Between the two upper and lower strips is the central strip with zero triple correlation values. This feature can be comprehended by examination of the turbulence diffusion mechanism. As shown in Figs. 3a–3d, the local highest values of Reynolds normal stresses $\overline{u'^2}$ and $\overline{v'^2}$ are located at the central strip of the shear layer. These high Reynolds normal stresses are transported to the upper and lower edges of the shear layer by v' through the turbulence diffusion mechanism. Because the upward transport to the upper edge requires positive v' fluctuations, u'^2v' and v'^3 therefore exhibit positive values in the upper strip of the shear layer. For the similar reason, u'^2v' and v'^3 exhibit negative values in the lower strip of the shear layer due to downward v' motion.

Because the measurements are conducted at the central span of the cavity flow field and the flow is 2D in the mean ($\overline{w} = \overline{w'} = 0$), $\overline{u'^7}$ and

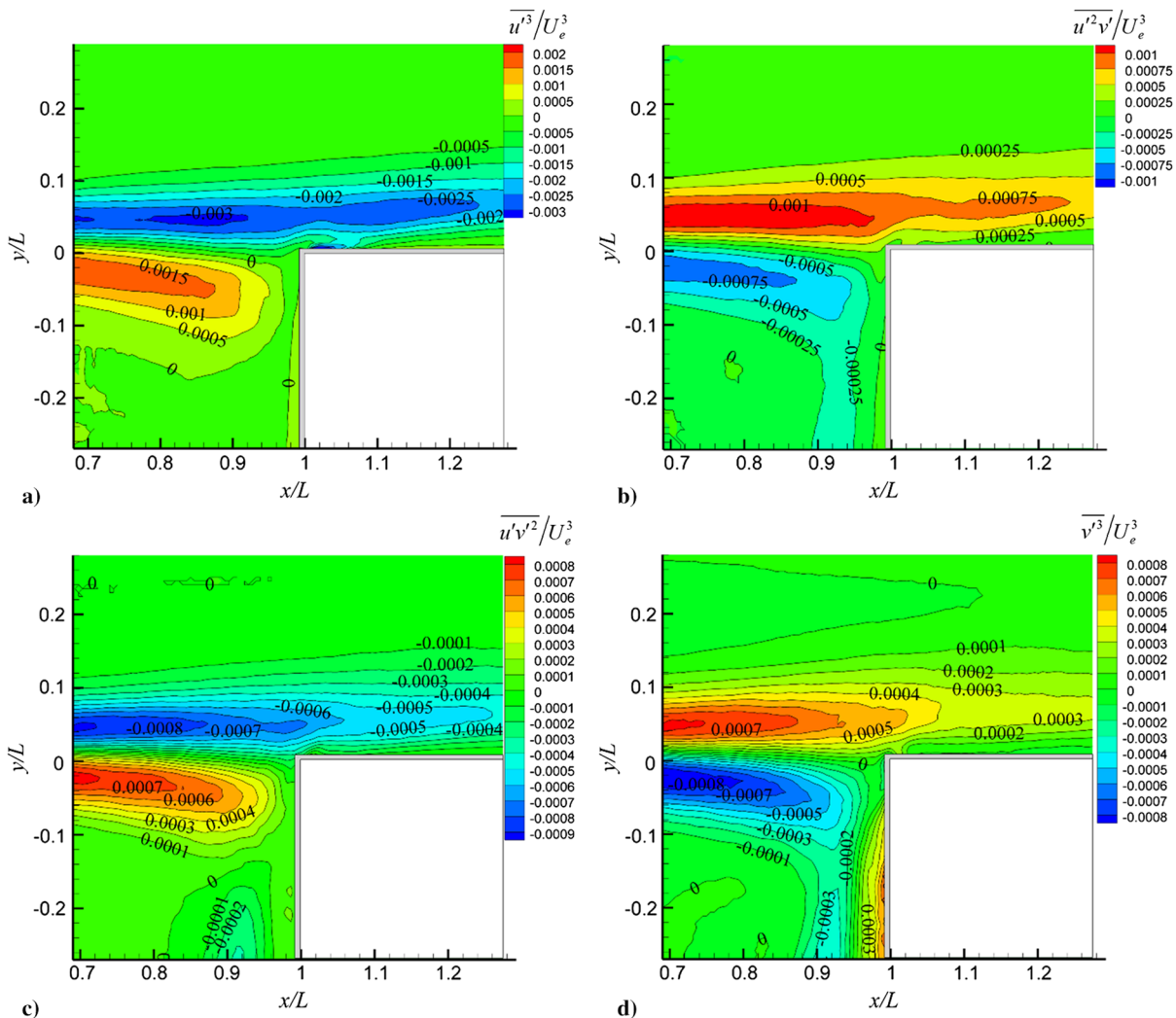


Fig. 7 Distribution of triple velocity correlations obtained at Reynolds number of 4.0×10^4 : a) u'^3 correlation; b) u'^2v' correlation; c) $u'v'^2$ correlation; and d) v'^3 correlation.

$\overline{v'}$ conform with the continuity equation as known from Reynolds decomposition. Thus, in a statistics sense, a positive v' fluctuation corresponds to a negative u' fluctuation, and vice versa. Therefore, in contrast to u'^3 and $u'v'^2$, reversed distribution patterns exist for u'^2v' and v'^3 distributions. Also please note that since statistically u' has higher fluctuation magnitude than v' as shown in Figs. 3a–3d, correspondingly u'^3 , u'^2v' , $u'v'^2$, and v'^3 exhibit a descending order of magnitudes in their distributions as shown in Fig. 7.

D. Pressure Diffusion Distribution and Comparison with Turbulence Diffusion and Turbulence Production Terms

Based on the distributions of the pressure–velocity and the triple velocity correlations, the corresponding pressure diffusion (also called the gradient of the Reynolds stress flux due to fluctuating pressure) and the turbulence diffusion of the Reynolds normal stresses of $\overline{u'^2}$ and $\overline{v'^2}$ can be evaluated and presented in Figs. 8 and 9 for the small field of view experiment, and Figs. 10 and 11 for the large field of view experiment, respectively. To gauge the distribution pattern and magnitude of the diffusion terms, the corresponding total in-plane turbulence production distributions are also shown in Figs. 8c, 9c, 10c, and 11c as an additional source for comparison. The total in-plane turbulence production is defined as

$$P = \underbrace{-\overline{u'v'}}_{\text{Shear production}} \left(\frac{\partial \overline{u}}{\partial y} + \frac{\partial \overline{v}}{\partial x} \right) + \underbrace{\left(-\overline{u'^2} \frac{\partial \overline{u}}{\partial x} - \overline{v'^2} \frac{\partial \overline{v}}{\partial y} \right)}_{\text{Dilatational production}} \quad (11)$$

To compare the composition of the in-plane turbulence production terms, distributions of both the shear production and the dilatational production terms are shown in Figs. 12a and 12b, respectively.

Comparing the diffusion distributions about the Reynolds normal stresses $\overline{u'^2}$ shown in Figs. 8a, 8b, 10a, and 10b, it can be seen that the turbulence diffusion of $\overline{u'^2}$ has higher magnitude than that for the pressure diffusion in the downstream half of the shear layer except the vicinity of the cavity trailing corner. However, this is not the case for the Reynolds normal stresses $\overline{v'^2}$ diffusions. As shown in Fig. 9b and especially Fig. 11b, in most of the downstream half of the shear layer, the pressure diffusion of $\overline{v'^2}$ has comparable or even higher magnitude than its local turbulence diffusion counterpart. The reason for the above differences in $\overline{u'^2}$ and $\overline{v'^2}$ pressure diffusion behavior is that the lateral gradients of $\overline{p'u'}$ and $\overline{p'v'}$ across the shear layer are much greater than their streamwise derivatives as shown in Figs. 4 and 5, conforming with the general thin shear layer characteristics.

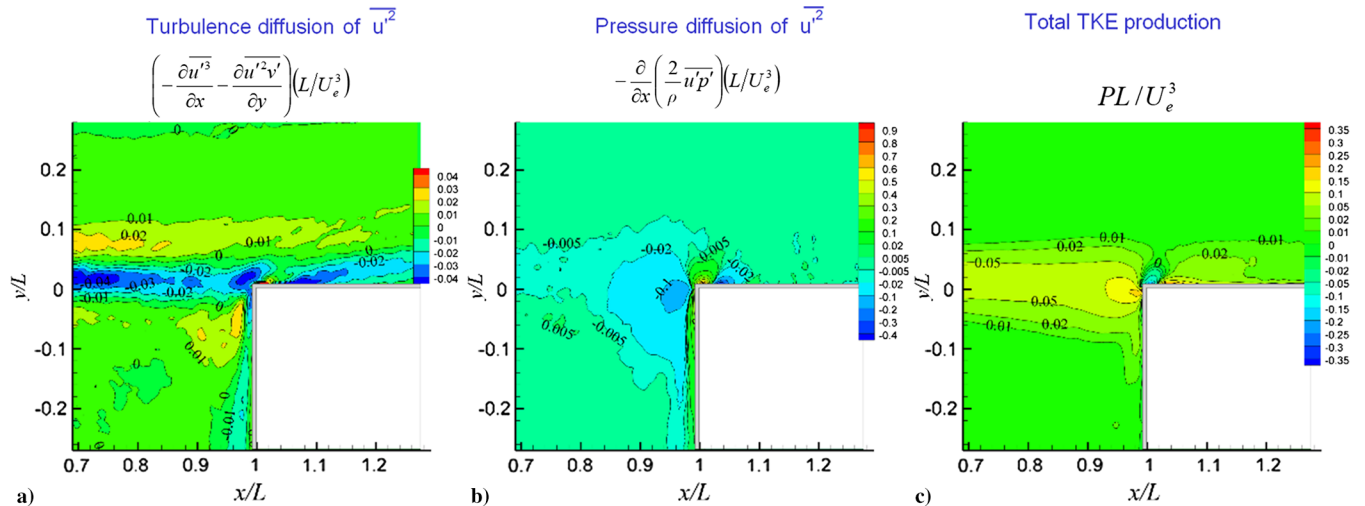


Fig. 8 Comparison of a) u -component turbulence diffusion, b) u -component pressure diffusion, and c) total turbulence kinetic energy production terms in a turbulent shear layer over an open cavity obtained at Reynolds number of 4.0×10^4 .

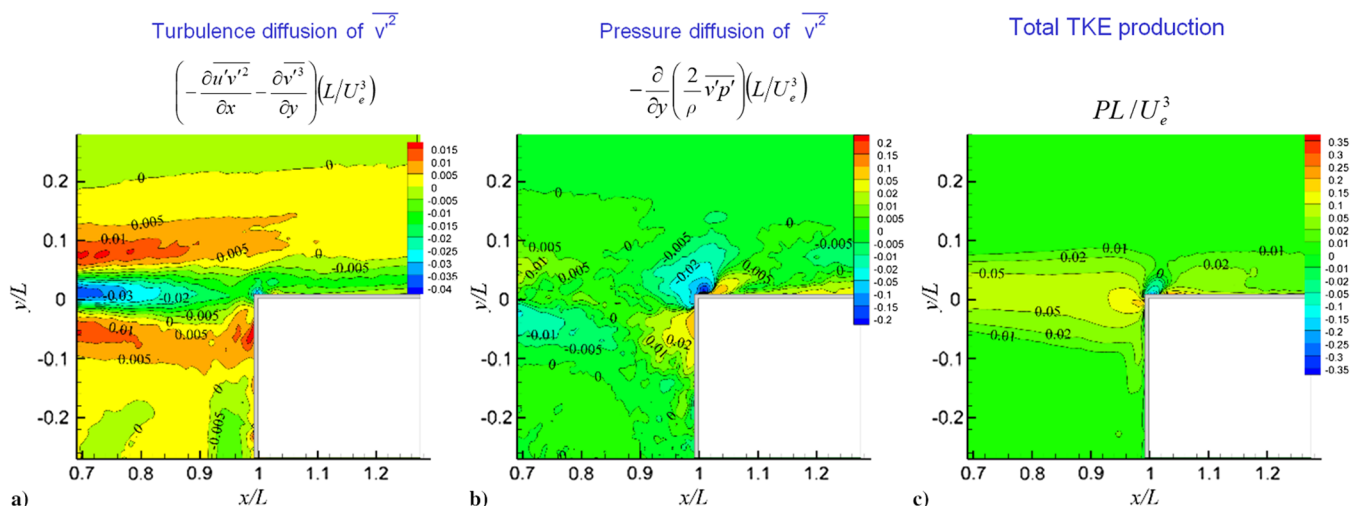


Fig. 9 Comparison of a) v -component turbulence diffusion, b) v -component pressure diffusion, and c) total turbulence kinetic energy production terms in a turbulent shear layer over an open cavity obtained at Reynolds number of 4.0×10^4 .

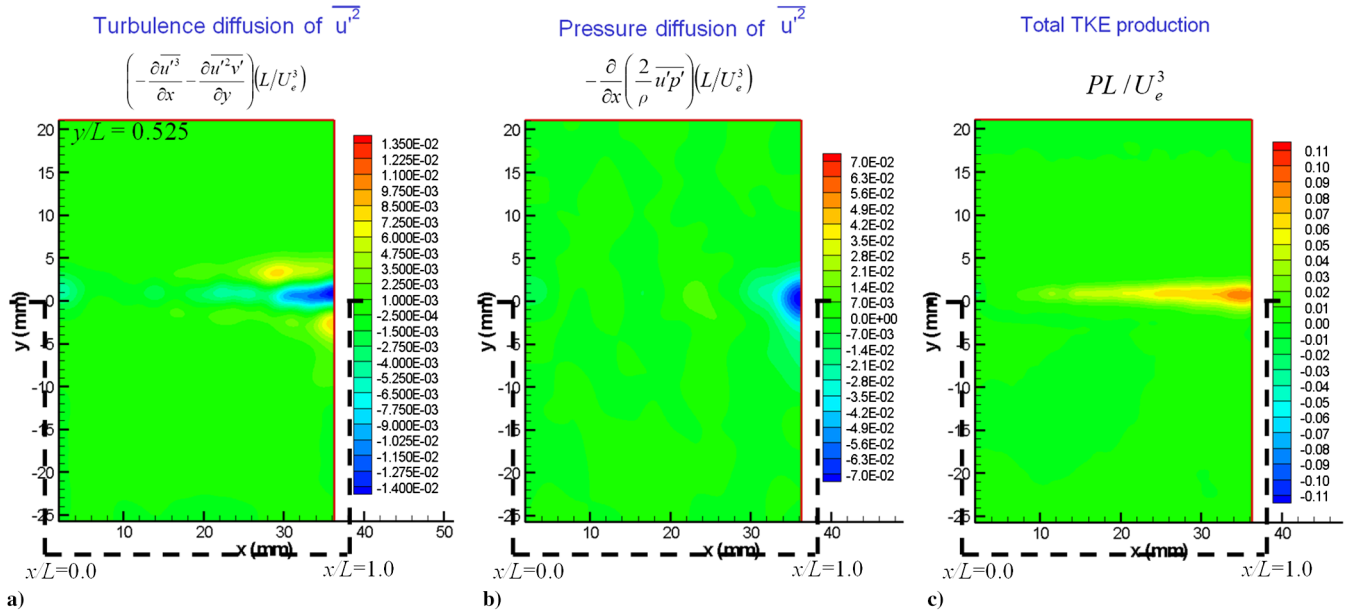


Fig. 10 Comparison of a) u -component turbulence diffusion, b) u -component pressure diffusion, and c) total turbulence kinetic energy production terms in a turbulent shear layer flow over an open cavity obtained at Reynolds number of 3.4×10^5 .

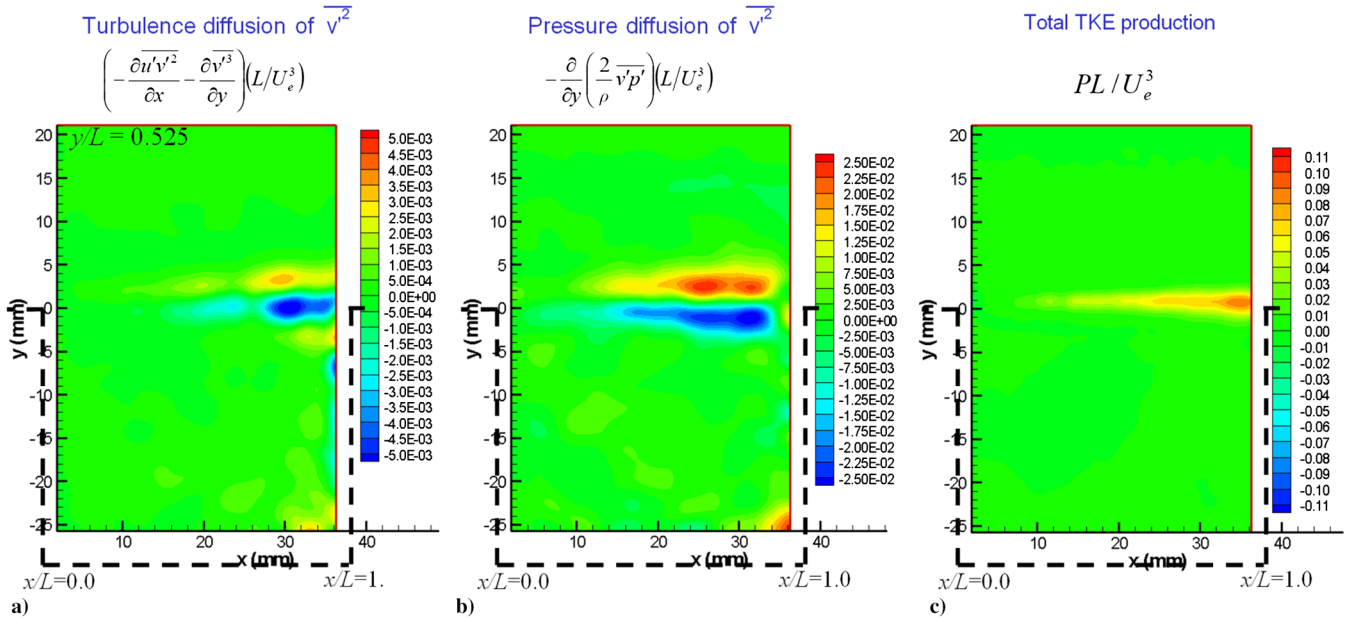


Fig. 11 Comparison of a) v -component turbulence diffusion, b) v -component pressure diffusion, and c) total turbulence kinetic energy production terms in a turbulent shear layer flow over an open cavity obtained at Reynolds number of 3.4×10^5 .

As a result, the pressure diffusion of v^2 exhibits a higher magnitude than that of the pressure diffusion of u^2 .

While it is negligible in the shear layer as shown in Figs. 8b and 10b, at places near the cavity trailing corner the u -component pressure diffusion is significant, and its magnitude is on the same order of those for the turbulence diffusion and the total turbulence production terms (Figs. 8 and 10), indicating that the u -component pressure diffusion terms cannot be neglected near the trailing corner in RANS simulations of turbulent cavity flows. Moreover, comparing Figs. 8b and 8c, it can be found that around the cavity trailing corner, the distribution patterns between the pressure diffusion of u^2 and the turbulence production terms have some similarity, but with opposite signs. This similarity between the two distribution patterns is in agreement with the general understanding of the diffusion mechanism; that is, newly generated turbulence is transported (diffused) to places

with lower concentration of newly generated turbulence, such as the area on top of the trailing corner where the turbulence production is negative.

Please note that peaks of the v -component pressure diffusion term are smaller in magnitude than those of the corresponding u -component pressure diffusion. The values of these two types of pressure diffusion terms are in opposite sign at corresponding locations surrounding the trailing corner of the cavity. As shown in Fig. 11b, beyond the field of view of Fig. 9b, around the mid-streamwise location of the shear layer, the v -component pressure diffusion is not negligible in comparison with the overall production rate.

The negative turbulence production above the trailing corner of the cavity shown in Figs. 8c and 9c, which tends to lead to the relaminarization phenomenon [71], is a result in part due to the local negative shear production shown Fig. 12a, and in part due to the local negative dilatational production shown in Fig. 12b. The local

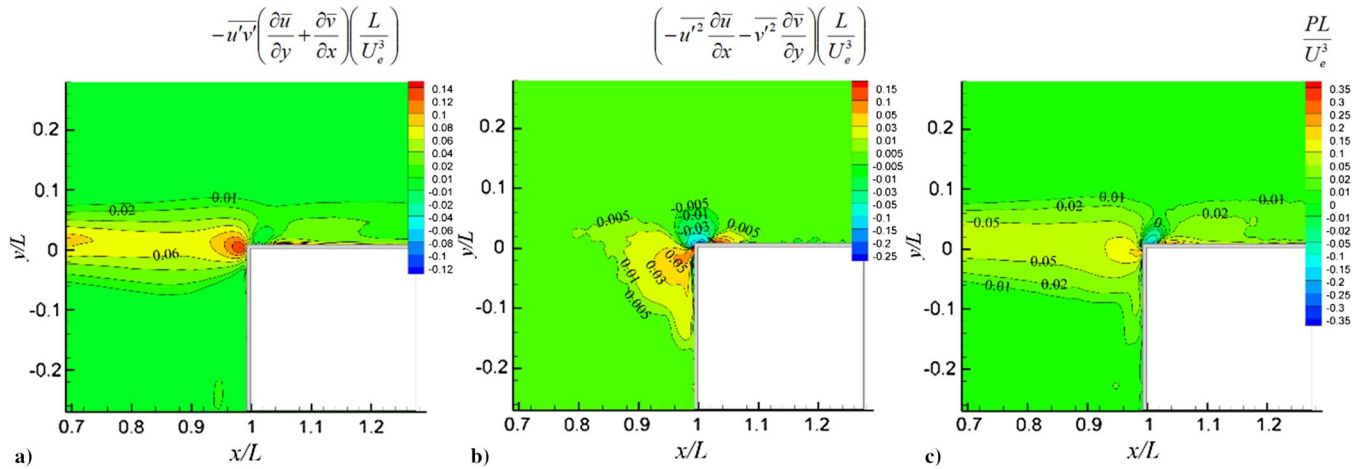


Fig. 12 Comparison of a) shear production, b) dilatational production, and c) total in-plane turbulence production terms in a turbulent shear layer over an open cavity obtained at Reynolds number of 4.0×10^4 .

negative shear production is a consequence of the local negative shear stress (Fig. 3f) on top of the trailing corner. For this cavity flow, as shown in Fig. 2f, a strong favorable pressure gradient region occurs around the tip of the cavity trailing corner, which causes a rapid streamwise acceleration, and consequently a strong negative dilatational production (Fig. 12b) there. The negative total in-plane turbulence production on top of the cavity trailing corner provides the foundation for a positive pressure diffusion of u'^2 occurring there as shown in Fig. 8b.

The turbulence diffusion of u'^2 in the shear layer appears to exhibit a roughly three-layered distribution pattern as shown in Figs. 8a and 10a. This three-layered pattern represents the results of the lateral turbulence transport of the fluctuation energy away from the maximum mean shear location in the central strip of the shear layer, where turbulence shear production is most intense, to places near the upper and lower edges of the shear layer, primarily through the lateral derivative term of the triple velocity correlation $-\overline{\partial u'^2 v' / \partial y}$, rather than the streamwise derivative term $-\overline{\partial u'^3 / \partial x}$, as revealed by the triple velocity correlation distributions shown in Figs. 7a and 7b. Thus, at the central strip of the shear layer, turbulence diffusion appears to have negative values, implying an energy loss, while near the upper and lower edges of the shear layer, turbulence diffusion appears to have positive values, meaning gains of fluctuation energy there. From Fig. 10a, it seems that the magnitude of this three-layered turbulence diffusion decreases in the upstream direction, which is consistent with the trend of a decreasing $|v'|$ as shown in Fig. 3c.

Clearly pressure-velocity correlations and subsequently the pressure diffusions have substantial impact on the dynamics of turbulence transport throughout the shear layer flow over the cavity. However, overall the distribution patterns between the turbulence diffusion and the pressure diffusion are considerably different, implying that the conventional practice of modeling these transport terms together, typically as Laplacians of the turbulent kinetic energy as shown in Eq. (7), may not be justifiable for this turbulent shear layer flow over a 2D open cavity. Furthermore, being of the same order of magnitude as the turbulence production terms, the effect of pressure diffusion on the evolution of streamwise velocity fluctuations cannot be neglected.

E. Comparisons of Velocity-Pressure-Gradient, Pressure-Rate-of-Strain, and Pressure Diffusion Terms

Figures 13 and 14 present the comparisons of the velocity-pressure-gradient, pressure-rate-of-strain, and pressure diffusion terms for the u - and v -components of Reynolds normal stress transport equations. All the terms shown in these two figures are calculated independently. The accuracy of the calculation is confirmed by plugging all measured terms into Eq. (5) and checking its validity. The common feature of all these three types of terms, for both the u - and v -components, is that their peak magnitudes and the highest variations occur in the area surrounding the tip of the trailing corner of the cavity, where the highest and periodic pressure gradient variations occur (see Figs. 2f and 3h for details about the pressure

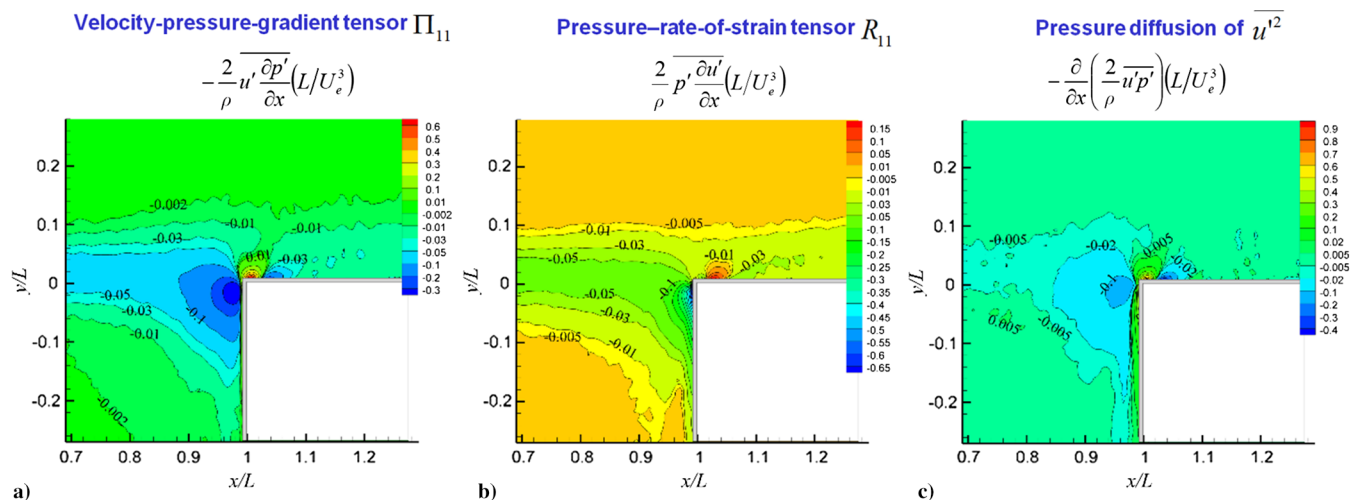


Fig. 13 Comparison of u -component of a) velocity-pressure-gradient tensor, b) pressure-rate-of-strain tensor, and c) pressure diffusion terms measured in the turbulent shear layer impinging on the trailing corner of an open cavity at Reynolds number of 4.0×10^4 .

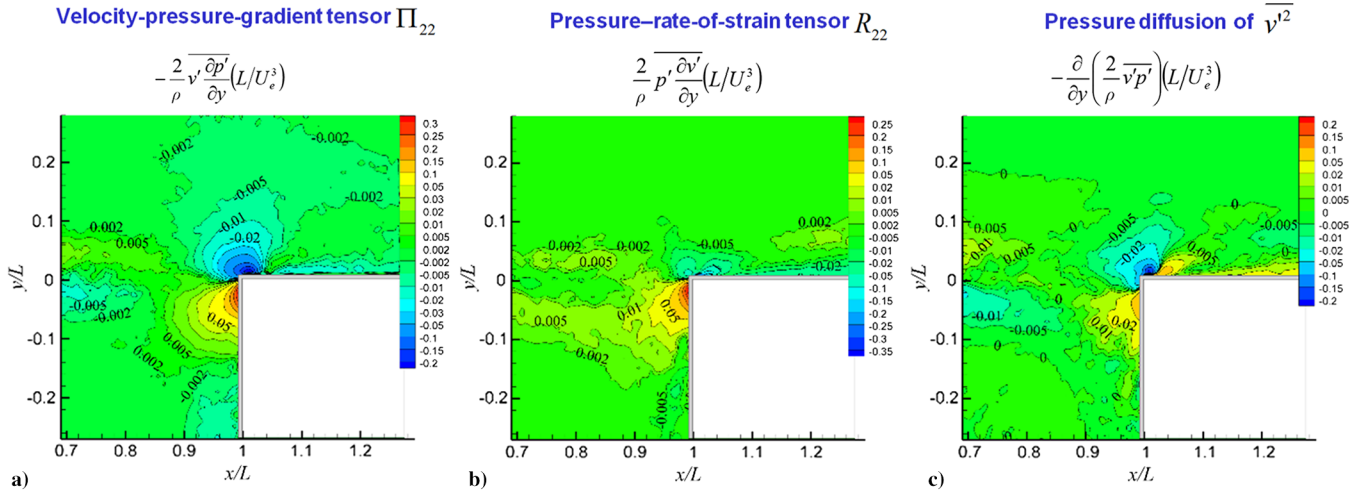


Fig. 14 Comparison of v -component of a) velocity-pressure-gradient tensor, b) pressure-rate-of-strain tensor, and c) pressure diffusion terms measured in the turbulent shear layer impinging on the trailing corner of an open cavity at Reynolds number of 4.0×10^4 .

field characterization around the corner). In the shear layer at the same locations, Π_{11} and R_{11} have values roughly one order of magnitude higher than their counterparts of the v -component terms.

It is interesting to note that R_{11} keeps a relatively strong negative value (approx. -0.05) throughout the shear layer. This value is strengthened significantly (approx. -0.65) at the impingement point on the trailing wall of the cavity. In contrast, R_{22} has a weak positive value in the shear layer. This is consistent with the magnitude distributions of the Reynolds normal stress u'^2 and v'^2 as shown in Figs. 3b and 3d, where the streamwise u -component fluctuation is clearly the dominant fluctuating velocity component in the shear layer, thus rendering its negative value in R_{11} , that is, implying the loss of energy from u'^2 to other components. Based on the above discussion, it seems that at least in the shear layer, major loss in the u -component fluctuation energy would be mainly absorbed by the spanwise w -component. Thus, 3D measurement techniques such as tomographic PIV may need to be employed in future experiment to bring this conjecture into a closure.

It is also interesting to note that close to the impingement point, the intercomponent fluctuation energy transfer that the v -component absorbs significantly increases up to about 0.25, that is, about 1/3 of the energy loss from the u -component fluctuation, as indicated in the R_{22} distribution. Considering the roughly -0.65 loss of the u -component fluctuation energy at that place, the amount of the fluctuation energy that the w -component absorbs at the same location can be inferred as 0.40 according to Eq. (6), implying that strong out-of-plane motion could occur near the impingement location. The strong out-of-plane motion might be a reason for the high uncertainty levels of the pressure-related statistics at that region, as will be shown later on in Sec. V.F.

In contrast, the intercomponent fluctuation energy transfer completely changes its scheme shortly downstream of the edge above the trailing corner, where R_{11} takes a positive value of approximately 0.15, and R_{22} a negative value of approximately -0.35 , meaning that the v -component fluctuation is losing energy and the u -component fluctuation is gaining energy. These variations are in agreement with the local u'^2 and v'^2 variations on top of the trailing corner as shown clearly in the insets of Figs. 3b and 3d, where u'^2 is gaining fluctuation energy along the streamwise direction while v'^2 at the same time is losing energy in the same region on top of the trailing corner. This is a good example demonstrating the key role that the pressure-rate-of-strain term plays in redistribution of energy among components of the turbulence normal stresses.

F. Convergence and Uncertainty Analysis

As mentioned in Sec. III, for the experiments conducted at Reynolds number of 4.0×10^4 , we have processed and analyzed 14 statistically independent datasets. Denote the mean value of a statistical quantity X for a dataset k as \bar{X}_k , where $k = 1, 2, \dots, N$

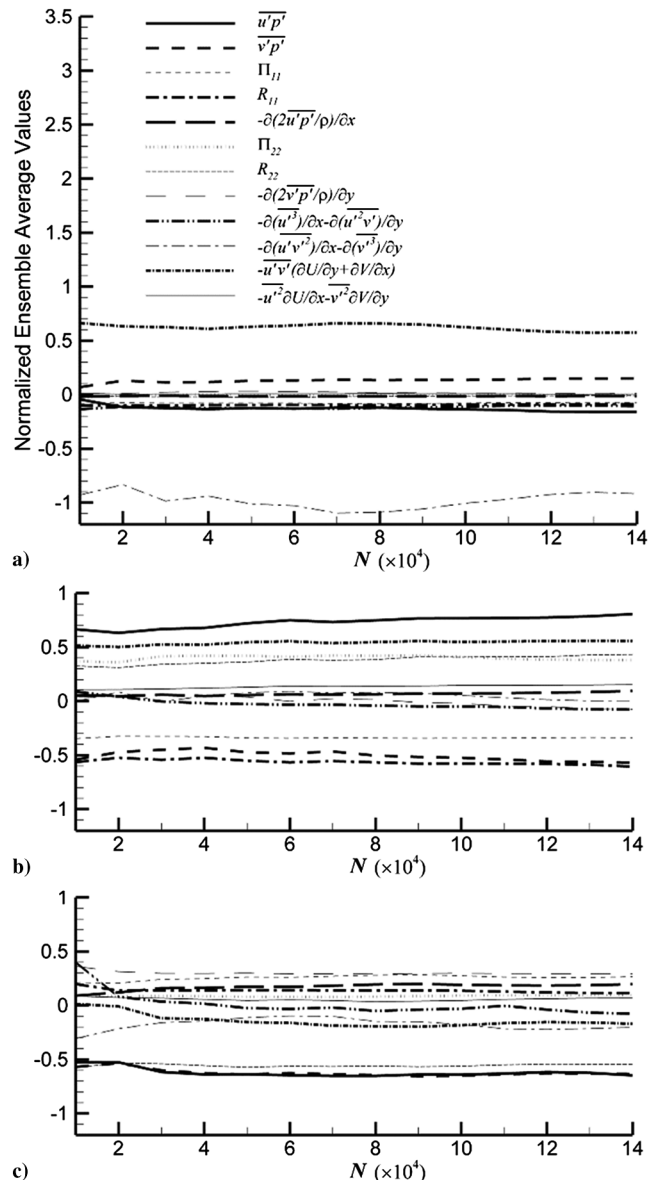


Fig. 15 Convergence of $\bar{X}/|\bar{X}|_{\max}$, that is, the ensemble average values \bar{X} for the measured statistical quantities normalized by their corresponding maximum absolute values $|\bar{X}|_{\max}$ within the field of view, with respect to the number of ensembles N (sample size = $N \times 10^4$) at a) point A, b) point B, and c) point C indicated in Fig. 3h for experiments conducted at Reynolds number of 4.0×10^4 .

represents the sequential number of the dataset, with N being the total number of datasets analyzed. Treating \bar{X}_k as a random number, the ensemble mean value \bar{X} based on averaging \bar{X}_k of N datasets of a statistical quantity X is then defined as

$$\bar{X} = \frac{1}{N} \sum_{k=1}^N \bar{X}_k \quad (12)$$

The standard deviation $S_{\bar{X}_k}$ of an arbitrary dataset mean \bar{X}_k can be calculated as

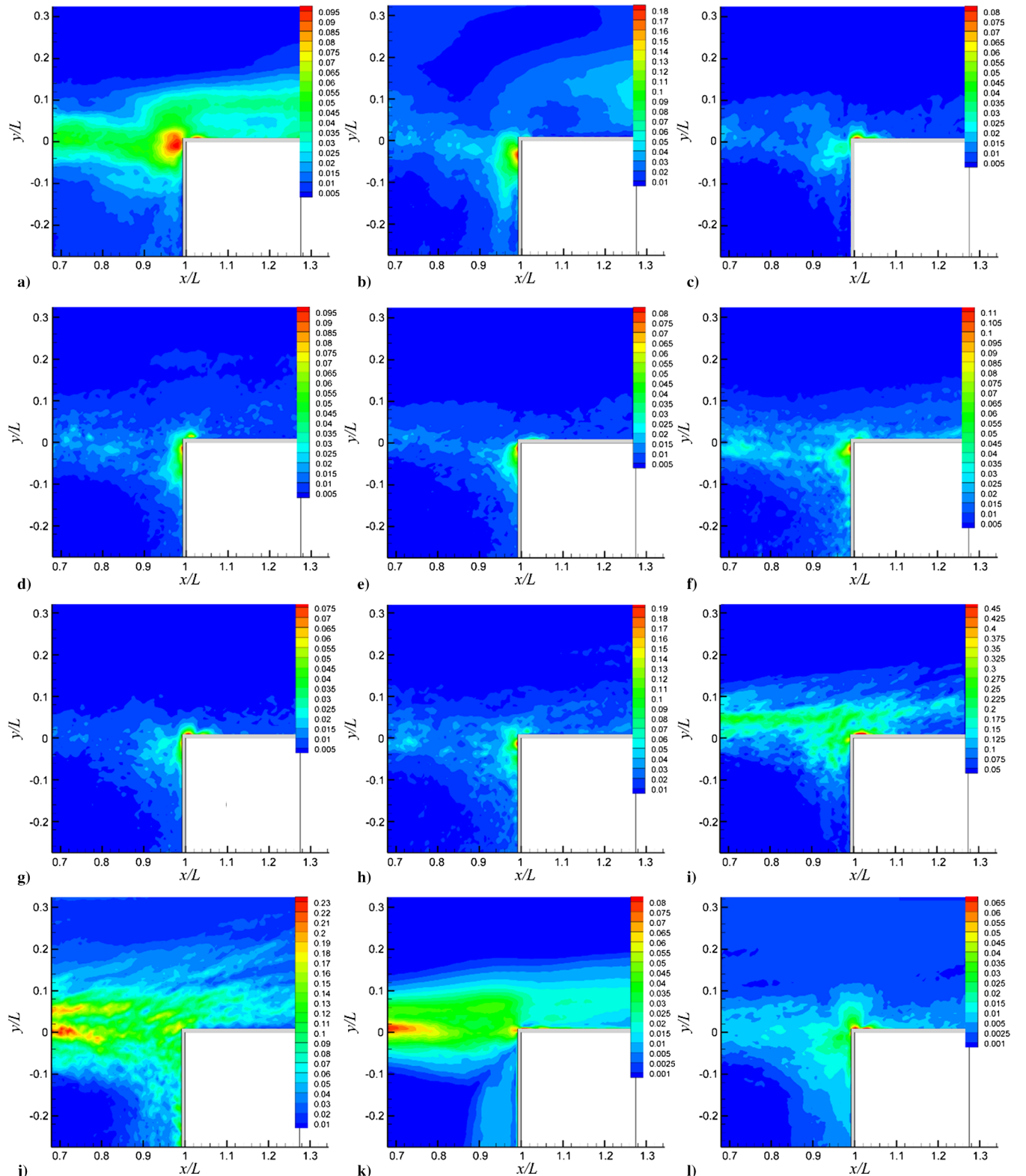


Fig. 16 Distribution of uncertainty magnitude $t_{13,95} S_{\bar{X}}$ at 95% confidence level normalized by the maximum absolute value $|\bar{X}|_{\max}$ within the field of view, that is, $t_{13,95} S_{\bar{X}}/|\bar{X}|_{\max}$ for a) $p'u'$; b) $p'v'$; c) Π_{11} , that is, $-2u'\partial p'/\partial x/\rho$; d) Π_{22} , that is, $-2v'\partial p'/\partial y/\rho$; e) R_{11} , that is, $-2p'\partial u'/\partial x/\rho$; f) R_{22} , that is, $-2p'\partial v'/\partial y/\rho$; g) u -component pressure diffusion, $-\partial(2p'u')/\partial x$; h) v -component pressure diffusion, $-\partial(2p'v')/\partial y$; i) u -component turbulence diffusion, $-\partial u'^3/\partial x - \partial u'^2 v'/\partial y$; j) v -component turbulence diffusion, $-\partial v'^3/\partial x - \partial v'^2 u'/\partial y$; k) shear turbulence production, $-\overline{u'v'}(\partial \bar{u}/\partial y + \partial \bar{v}/\partial x)$; and l) dilatational turbulence production, $-\overline{u'^2}(\partial \bar{u}/\partial x) - \overline{v'^2}(\partial \bar{v}/\partial y)$ in a turbulent shear layer flow over a cavity at Reynolds number of 4.0×10^4 .

$$S_{\bar{X}_k} = \sqrt{\frac{1}{N-1} \sum_{k=1}^N (\bar{X}_k - \bar{X})^2} \quad (13)$$

Subsequently, the standard deviation $S_{\bar{X}}$ of the ensemble mean value \bar{X} can be obtained as

$$S_{\bar{X}} = \frac{1}{\sqrt{N}} S_{\bar{X}_k} = \sqrt{\frac{1}{N(N-1)} \sum_{k=1}^N (\bar{X}_k - \bar{X})^2} \quad (14)$$

The uncertainty range over which the possible values of the true ensemble mean value of quantity X might lie at some probability level (a.k.a., confidence level) $P\%$ is given as

$$\bar{X} \pm t_{\nu, P} S_{\bar{X}} (P\%) \quad (15)$$

where $\nu = N - 1$ is the degree of freedom for the standard deviation, and t is the Student's t variable. For the small field of view experiment, $N = 14$ and correspondingly, $t_{13,95} = 2.160$.

Figure 15 examines the convergence of $\bar{X}/|\bar{X}|_{\max}$ with respect to the number of ensembles N for a variety of statistical quantities presented in this paper at points A, B, and C as indicated in Fig. 3h for experiments conducted at Reynolds number of 4.0×10^4 , with $|\bar{X}|_{\max}$ being the maximum absolute value of the ensemble mean of quantity X within the field of view. From this figure it can be seen that different statistical quantities tend to have different rate for convergence. However, when the number of the ensemble is increased to about 12–14, statistical quantities, including the pressure–velocity correlation, pressure diffusion, velocity–pressure–gradient correlation, and pressure–rate-of-strain, all exhibit a reasonable degree of convergence. It seems that except the v -component turbulence diffusion term and the shear production term, most of the quantities presented in the figure tend to converge quickly in the shear layer at location A. Ensemble mean values for statistical quantities at locations B and C, that is, around the cavity trailing corner, appear to have noticeable oscillations for small ensemble sizes with $N < 4$. However, when $N > 4$, it seems that the ensemble mean values for most quantities at those locations appear to converge rather quickly.

Distribution of uncertainty magnitude $t_{13,95} S_{\bar{X}}$ at 95% confidence level normalized by $|\bar{X}|_{\max}$ for a variety of statistical quantities is shown in Fig. 16. Corresponding to this figure, characteristic maximum uncertainty ranges ($\pm t_{13,95} S_{\bar{X}}$) of the measured statistical quantity ensemble average values are summarized in Table 2. As shown in Fig. 16, the uncertainty magnitudes for all the measured

quantities are heavily location dependent in the flow field. Except the v -component turbulence diffusion $-\partial u'v'^2/\partial x - \partial v'^3/\partial y$ and the shear production $-u'v'(\partial \bar{u}/\partial y + \partial \bar{v}/\partial x)$ terms, the maximum uncertainty magnitudes in the entire flow field for all the rest quantities shown in Fig. 16 occur around the cavity trailing corner. As mentioned in Sec. V.E, the high uncertainty levels of the pressure-related statistics at the region around the trailing corner might be a result of the strong out-of-plane motion in this region. Again this conjecture could be verified by 3D measurement data in future experiment.

For the v -component turbulence diffusion term and the shear production term, the maximum uncertainty magnitudes occur in the shear layer. Away from the viscous-dominated regions, the uncertainty magnitude diminishes. Comparing the distributions shown in Figs. 4, 8, 9, and 12–14, it seems that these uncertainty distribution features are to some extent related to the distributions of the statistical quantities themselves, indicating that high magnitudes of turbulence quantities are roughly associated with high levels of measurement uncertainty. As summarized in Table 2, both the u -component turbulence diffusion term $-\partial u'^3/\partial x - \partial u'^2v'/\partial y$ and the v -component turbulence diffusion term $-\partial u'v'^2/\partial x - \partial v'^3/\partial y$ have higher peak relative uncertainty magnitudes (e.g., $>20\%$ in shear layer) at representative locations than other statistical quantities. The reason for this feature is that, unlike other quantities, the peak reference values for both the u - and the v -components of the turbulence diffusion terms are located in the shear layer, rather than the places around the cavity trailing corner. Unlike all the pressure-related terms and the dilatational production terms, the turbulence diffusion terms do not have a mechanism to intensify their magnitudes around the cavity trailing corner. Therefore, their peak ensemble mean values occurring in the shear layer have relatively weak magnitudes (0.059 and 0.038) comparing to the peak ensemble mean values of other quantities (typically 0.2–0.7, an order of magnitude higher than the former), as shown in Table 2.

The effects of out-of-plane motions on the measurement are estimated using the following approach: First, we use the continuity equation $\partial w/\partial z = -(\partial u/\partial x + \partial v/\partial y)$ to estimate the mean out-of-plane velocity-gradients $\partial w/\partial z$ and the rms values of $\partial w/\partial z$. It turns out that in most places, including the shear layer, $\partial w/\partial z$ is zero, which means that the mean flow is 2D, and implies $\bar{w} = 0$ in the present setting. Thus, the contribution of spanwise motions to the streamwise momentum equation, is $w' \partial u'/\partial z$. Our data show that $\partial w/\partial z|_{\text{rms}}$ has roughly the same magnitude as that of $\partial u/\partial x|_{\text{rms}}$ in the shear layer. Thus, assuming that $\partial u/\partial z|_{\text{rms}} \approx \partial w/\partial z|_{\text{rms}}$, enables us to estimate $\partial u/\partial z|_{\text{rms}}$ using $\partial u/\partial x|_{\text{rms}}$. According to Chang et al. [72], who used LES to investigate an incompressible open cavity shear layer flow, w_{rms} has similar profile

Table 2 Characteristic maximum uncertainty range ($\pm t_{13,95} S_{\bar{X}}$) of ensemble average values for the measured statistical quantities at 95% confidence level, normalized by their corresponding maximum absolute values ($|\bar{X}|_{\max}$) within the field of view, that is, $\pm t_{13,95} S_{\bar{X}}/|\bar{X}|_{\max}$, for experiments at Reynolds number of 4.0×10^4

Statistical quantity \bar{X}	$\pm t_{13,95} S_{\bar{X}}/ \bar{X} _{\max}$ in shear layer, %	$\pm t_{13,95} S_{\bar{X}}/ \bar{X} _{\max}$ in front of trailing corner, %	$\pm t_{13,95} S_{\bar{X}}/ \bar{X} _{\max}$ above trailing corner, %	$ \bar{X} _{\max}$ within FOV
$(\bar{p}'u')/(\rho U_c^3)$	± 5.0	± 9.6	± 8.0	0.0056
$(\bar{p}'v')/(\rho U_c^3)$	± 4.1	± 17.9	± 5.6	0.0029
$(-2\bar{u}'\partial p'/\partial x)/\rho(L/U_c^3)$, i.e., Π_{11}	± 1.8	± 3.0	± 8.0	0.69
$(-2\bar{v}'\partial p'/\partial y)/\rho(L/U_c^3)$, i.e., Π_{22}	± 2.4	± 9.5	± 8.3	0.27
$(-2\bar{p}'\partial u'/\partial x)/\rho(L/U_c^3)$, i.e., R_{11}	± 1.8	± 8.1	± 3.3	0.69
$(-2\bar{p}'\partial v'/\partial y)/\rho(L/U_c^3)$, i.e., R_{22}	± 3.7	± 10.8	± 5.2	0.29
$(-\partial(2\bar{p}'u'/\rho)/\partial x)(L/U_c^3)$	± 1.5	± 6.9	± 7.7	0.75
$(-\partial(2\bar{p}'v'/\rho)/\partial y)(L/U_c^3)$	± 5.4	± 18.9	± 8.1	0.21
$(-\partial u'^3/\partial x - \partial u'^2v'/\partial y)(L/U_c^3)$	± 25.1	± 34.5	± 45.6	0.059
$(-\partial u'v'^2/\partial x - \partial v'^3/\partial y)(L/U_c^3)$	± 22.5	± 10.8	± 11.0	0.038
$(-\bar{u}'v'(\partial \bar{u}/\partial y + \partial \bar{v}/\partial x))(L/U_c^3)$	± 7.9	± 6.7	± 6.5	0.138
$(-\bar{u}'^2(\partial \bar{u}/\partial x) - \bar{v}'^2(\partial \bar{v}/\partial y))(L/U_c^3)$	± 0.9	± 5.6	± 6.7	0.232
Total in-plane production (PL/U_c^3)	± 5.9	± 6.0	± 9.5	0.211

and magnitude as that of v_{rms} . Combining this information, we estimate that $w_{\text{rms}} \partial u / \partial z|_{\text{rms}} \approx v_{\text{rms}} \partial u / \partial x|_{\text{rms}}$. Calculations, based on four sets of data near the trailing corner, show that $v_{\text{rms}} \partial u / \partial x|_{\text{rms}}$ is not more than 14% of the measured fluctuations of $Du/Dt|_{\text{rms}}$ in the shear layer near the trailing corner, and 5% outside of the shear layer. This result is consistent in terms of order of magnitude with the uncertainty calculations shown in Fig. 16 and Table 2.

VI. Conclusions

Pressure–velocity correlation, pressure diffusion, pressure–rate-of-strain, and velocity–pressure-gradient tensors have been measured in a turbulent shear layer flow over a 2D open cavity at a Reynolds number of 4.0×10^4 based on the cavity length. The analysis is also augmented with comparisons with experimental data obtained at a higher Reynolds number of 3.4×10^5 . To the best of our knowledge, this is the first time that these important terms are experimentally measured in a cavity shear layer flow. The measurement results lead to the following conclusions:

In most of the shear layer, u' and p' are negatively correlated. However, as the flow approaches the trailing edge of the cavity, due to the presence of the adverse pressure gradient, $p'u'$ changes its sign, creating a positive peak just upstream of the trailing edge. Immediately above the trailing corner, $p'u'$ changes its sign again, appearing with a negative value. As for the $p'v'$ correlation, p' and v' are positively correlated in most of the shear layer. Because of the adverse pressure gradient, $p'v'$ takes a negative value in the impingement area of the trailing corner, and remains as negatively correlated above the trailing corner due to flow acceleration there.

The probability density function profiles of the pressure–velocity correlation and their corresponding skewness and kurtosis characteristics indicate that for the majority of time in the shear layer and around the cavity trailing corner, pressure and velocity are not correlated. It is the less-frequent flow events that alter the shape of the PDF profiles and subsequently determine the mean value of the pressure–velocity correlation.

The turbulence diffusion of u'^2 has higher magnitude than the pressure diffusion of u'^2 in the shear layer. Away from the corner, pressure diffusion of u'^2 is negligible. However, in most of the downstream half of the shear layer, the pressure diffusion of v'^2 has comparable or even higher magnitude than its local turbulence diffusion counterpart. Close to the corner, both u - and v -components of pressure diffusion are significant, and their magnitudes are on the same order as that of the total turbulence production term, indicating that the pressure diffusion terms cannot be neglected near the cavity trailing edge in RANS simulations.

The distribution patterns of the turbulence diffusion and the pressure diffusion are considerably different. Thus the conventional practice of modeling the transport terms all together as Laplacians of the turbulent kinetic energy shown in Eq. (7) is not justifiable at least for the present geometry.

The u - and the v -component pressure diffusion terms have opposite signs at corresponding locations surrounding the trailing corner of the cavity, where the peaks of the v -component pressure diffusion are smaller in magnitude than those of the u -component counterparts.

In the shear layer, Π_{11} and R_{11} have values roughly one order of magnitude higher than their counterparts of the v -component terms. R_{11} keeps a relatively strong negative value throughout the shear layer and strengthens significantly at the impingement point. In contrast, R_{22} has a small positive value in the shear layer. This trend is consistent with the magnitudes of the Reynolds normal stresses u'^2 and v'^2 distributions in the flow field. According to the intercomponent fluctuation energy balance, in the shear layer major loss in the u -component fluctuation energy would be mainly absorbed by the spanwise w -component fluctuation.

Close to the impingement point, the amount of the intercomponent fluctuation energy transfer that the v -component fluctuation receives significantly increases up to about 1/3 of the energy loss from the u -component fluctuation. As indicated by the energy transfer balance, the spanwise w -component fluctuation energy absorbed

from the u -component fluctuation energy loss also significantly increases near the impingement point, implying strong out-of-plane motion in that region.

The intercomponent fluctuation energy transfer completely changes its distribution on top of the trailing corner, where R_{11} takes a positive value and R_{22} a negative one, indicating that the u -component fluctuation is gaining while the v -component fluctuation is losing energy. This trend is again consistent with the local Reynolds normal stress u'^2 and v'^2 variations.

The uncertainty magnitude distributions for the turbulence statistical quantities investigated are location dependent. The maximum uncertainty magnitudes in the entire flow field for all the pressure-related terms occur around the cavity trailing corner. In contrast, the maximum uncertainty magnitudes for the v -component turbulence diffusion term and the shear turbulence production term occur in the shear layer. The strong w -component out-of-plane motion near the trailing corner might be the reason that contributes to the high uncertainty level of pressure-related statistics there. To verify this conjecture, 3D measurement techniques such as tomographic PIV may need to be employed in future experiment.

The complicated intercomponent energy transfer process described above clearly shows the challenge (and perhaps opportunities) that turbulence modeling for Reynolds stress transport faces in the situation of turbulent shear layer flow over an open cavity in particular, and separation and reattachment flow in general (e.g., impingement of a shear flow on a surface, such as wake ingestion in a rotor passage). Clearly the velocity–pressure-gradient tensor, the pressure diffusion and the pressure–rate-of-strain distributions have substantial impact on the dynamics of turbulence transport throughout the shear layer. The complex behaviors of the pressure-related turbulence transport terms around the impingement area are intriguing and apparently need further investigation in future so as to better understand the flow physics there.

Acknowledgments

The research was sponsored in part by the Office of Naval Research (Ki-Han Kim and Deborah Nalchajian are the program officers), and in part by National Science Foundation grant CBET-1438203 (R. Joslin is the program director). The financial support from the UGP program of the San Diego State University is also gratefully acknowledged. The insightful comments from the reviewers of the paper are also highly appreciated. X. Liu thanks Flint O. Thomas and Robert C. Nelson for their encouragement during the process of the pressure-related research.

References

- [1] Oden, J. T., Belytschko, T., Fish, J., Hughes, T. J. R., Johnson, C., Keyes, D., Laub, A., Petzold, L., Srolovitz, D., and Yip, S., et al., "Simulation-Based Engineering Science—Revolutionizing Engineering Science Through Simulation," National Science Foundation, Washington, D.C., 2006, https://www.nsf.gov/pubs/reports/sbes_final_report.pdf.
- [2] Slotnick, J., Khodadoust, A., Alonso, J., Darmofal, D., Gropp, W., Lurie, E., and Mavriplis, D., "CFD Vision 2030 Study: A Path to Revolutionary Computational Aerodynamics," NASA CR-2014-218178, 2014.
- [3] Wilcox, D. C., *Turbulence Modeling for CFD*, 3rd ed., DCW Industries, La Canada, CA, 2006.
- [4] Liu, X., and Katz, J., "Measurements of Pressure Distribution by Integrating the Material Acceleration," *Proceedings of the 5th International Symposium on Cavitation (Cav2003)* [CD-ROM], Paper Cav03-GS-14-001, Monbu Kagakusho, Japan, Nov. 2003.
- [5] Liu, X., and Katz, J., "Instantaneous Pressure and Material Acceleration Measurements Using a Four Exposure PIV System," *Experiments in Fluids*, Vol. 41, No. 2, Aug. 2006, pp. 227–240. doi:10.1007/s00348-006-0152-7
- [6] Liu, X., and Katz, J., "A Comparison of Cavitation Inception Index Measurements to the Spatial Pressure Distribution Within a 2D Cavity Shear Flow," *5th Joint ASME/JSME Fluids Engineering Conference*, ASME Paper FEDSM2007-37090, New York, 2007, pp. 329–339. doi:10.1115/FEDSM2007-37090
- [7] Liu, X., and Katz, J., "Cavitation Phenomena Occurring due to Interaction of Shear Layer Vortices with the Trailing Corner of a 2D

- Open Cavity,” *Physics of Fluids*, Vol. 20, No. 4, April 2008, Paper 041702.
doi:10.1063/1.2897320
- [8] Liu, X., and Katz, J., “Vortex-Corner Interactions in a Cavity Shear Layer Elucidated by Time Resolved Measurements of the Pressure Field,” *Journal of Fluid Mechanics*, Vol. 728, Aug. 2013, pp. 417–457. doi:10.1017/jfm.2013.275
- [9] van Oudheusden, B. W., “Principles and Application of Velocimetry-Based Planar Pressure Imaging in Compressible Flows with Shocks,” *Experiments in Fluids*, Vol. 45, No. 4, 2008, pp. 657–674. doi:10.1007/s00348-008-0546-9
- [10] Ragni, D., Ashok, A., Van Oudheusden, B. W., and Scarano, F., “Surface Pressure and Determination of a Transonic Aerofoil Based on Particle Image Velocimetry,” *Measurement Science and Technology*, Vol. 20, No. 7, July 2009, Paper 074005. doi:10.1088/0957-0233/20/7/074005
- [11] Joshi, P., Liu, X., and Katz, J., “Effect of Mean and Fluctuating Pressure Gradients on Boundary Layer Turbulence,” *Journal of Fluid Mechanics*, Vol. 748, June 2014, pp. 36–84. doi:10.1017/jfm.2014.147
- [12] Liu, X., Moreto, J. R., and Siddle-Mitchel, S., “Instantaneous Pressure Reconstruction from Measured Pressure Gradient Using Rotating Parallel Ray Method,” *54th AIAA Aerospace Sciences Meeting, AIAA SciTech*, AIAA Paper 2016-1049, Jan. 2016. doi:10.2514/6.2016-1049
- [13] Zhang, C., Wang, J., Blake, W., and Katz, J., “Deformation of a Compliant Wall in a Turbulent Channel Flow,” *Journal of Fluid Mechanics*, Vol. 823, July 2017, pp. 345–390. doi:10.1017/jfm.2017.299
- [14] Dabiri, J. O., Bose, S., Gemmell, B. J., Colin, S. P., and Costello, J. H., “An Algorithm to Estimate Unsteady and Quasi-Steady Pressure Fields from Velocity Field Measurements,” *Journal of Experimental Biology*, Vol. 217, No. 3, 2014, pp. 331–336. doi:10.1242/jeb.092767
- [15] Wang, Z., Gao, Q., Wang, C., Wei, R., and Wang, J., “An Irrotation Correction on Pressure Gradient and Orthogonal-Path Integration for PIV-Based Pressure Reconstruction,” *Experiments in Fluids*, Vol. 57, No. 6, 2016, p. 104. doi:10.1007/s00348-016-2189-6
- [16] de Kat, R., and van Oudheusden, B. W., “Instantaneous Planar Pressure from PIV: Analytic and Experimental Test-Cases,” *15th International Symposium on Applications of Laser Techniques to Fluid Mechanics [CD-ROM]*, Lisbon, July 2010.
- [17] de Kat, R., and van Oudheusden, B. W., “Instantaneous Planar Pressure Determination from PIV in Turbulent Flow,” *Experiments in Fluids*, Vol. 52, No. 5, 2012, pp. 1089–1106. doi:10.1007/s00348-011-1237-5
- [18] Violato, D., Moore, P., and Scarano, F., “Lagrangian and Eulerian Pressure Field Evaluation of Rod-Airfoil Flow from Time-Resolved Tomographic PIV,” *Experiments in Fluids*, Vol. 50, No. 4, April 2011, pp. 1057–1070. doi:10.1007/s00348-010-1011-0
- [19] Auteri, F., Carina, M., Zagaglia, D., Montagnon, D., Libertine, G., Mars, C. B., and Zanetti, A., “A Novel Approach for Reconstructing Pressure from PIV Velocity Measurements,” *Experiments in Fluids*, Vol. 56, No. 45, Feb. 2015, pp. 1–16. doi:10.1007/s00348-015-1912-z
- [20] Charonko, J. J., King, C. V., Smith, B. L., and Vlachos, P. P., “Assessment of Pressure Field Calculations from Particle Image Velocimetry Measurements,” *Measurements Science and Technology*, Vol. 21, No. 10, Oct. 2010, Paper 105401. doi:10.1088/0957-0233/21/10/105401
- [21] van Oudheusden, B. W., “PIV-Based Pressure Measurement,” *Measurements Science and Technology*, Vol. 24, No. 3, March 2013, Paper 032001. doi:10.1088/0957-0233/24/3/032001
- [22] Jeon, Y. J., Chatellier, L., Beaudoin, A., and David, L., “Least-Square Reconstruction of Instantaneous Pressure Field Around a Body Based on a Directly Acquired Material Acceleration in Time-Resolved PIV,” *11th International Symposium on Particle Image Velocimetry—PIV15*, Santa Barbara, CA, Sept. 2015, https://www.researchgate.net/profile/Laurent_David/publication/281898433_Leastsquare_reconstruction_of_instantaneous_pressure_field_around_a_body_based_on_a_directly_acquired_material_acceleration_in_time-resolved_PIV/links/55fd0ecb08aeafc8ac55598d.pdf.
- [23] Wang, C. Y., Gao, Q., Wei, R. J., Li, T., and Wang, J. J., “Spectral Decomposition-Based Fast Pressure Integration Algorithm,” *Experiments in Fluids*, Vol. 58, No. 7, 2017, p. 84. doi:10.1007/s00348-017-2368-0
- [24] Tronchin, T., David, L., and Farcy, A., “Loads and Pressure Evaluation of the Flow Around a Flapping Wing from Instantaneous 3D Velocity Measurements,” *Experiments in Fluids*, Vol. 56, No. 1, 2015, p. 7. doi:10.1007/s00348-014-1870-x
- [25] Neeteson, N. J., and Rival, D. E., “Pressure-Field Extraction on Unstructured Flow Data Using a Voronoi Tessellation-Based Networking Algorithm: A Proof-of-Principle Study,” *Experiments in Fluids*, Vol. 56, No. 2, 2015, p. 44. doi:10.1007/s00348-015-1911-0
- [26] Schanz, D., Gesemann, S., and Schröder, A., “Shake-The-Box: Lagrangian Particle Tracking at High Particle Image Densities,” *Experiments in Fluids*, Vol. 57, No. 5, 2016, p. 70. doi:10.1007/s00348-016-2157-1
- [27] Huhn, F., Schanz, D., Gesemann, S., and Schroder, A., “FFT Integration of Instantaneous 3D Pressure Gradient Fields Measured by Lagrangian Particle Tracking in Turbulent Flows,” *Experiments in Fluids*, Vol. 57, No. 9, 2016, p. 151. doi:10.1007/s00348-016-2236-3
- [28] van Gent, P. L., Michaelis, D., van Oudheusden, B. W., Weiss, P.-É., de Kat, R., Laskari, A., Jeon, Y. J., David, L., Schanz, D., and Huhn, F., et al., “Comparative Assessment of Pressure Field Reconstructions from Particle Image Velocimetry Measurements and Lagrangian Particle Tracking,” *Experiments in Fluids*, Vol. 58, No. 4, 2017, p. 33. doi:10.1007/s00348-017-2324-z
- [29] de Kat, R., and Ganapathisubramani, B., “Pressure from Particle Image Velocimetry for Convective Flows: A Taylor’s Hypothesis Approach,” *Measurements Science and Technology*, Vol. 24, No. 2, 2013, Paper 024002. doi:10.1088/0957-0233/24/2/024002
- [30] Moin, P., and Mahesh, K., “Direct Numerical Simulation: A Tool in Turbulence Research,” *Annual Review of Fluid Mechanics*, Vol. 30, No. 1, 1998, pp. 539–578. doi:10.1146/annurev.fluid.30.1.539
- [31] Moser, R., Rogers, M., and Ewing, D., “Self-Similarity of Time-Evolving Plane Wakes,” *Journal of Fluid Mechanics*, Vol. 367, July 1998, pp. 255–289. doi:10.1017/S0022112098001426
- [32] Rumsey, C. L., and Jeyapaul, E., “Pressure–Strain and Near-Wall Modeling for Two-Dimensional Separated Flows,” *Proceedings of the Summer Program 2012*, Center for Turbulence Research, Stanford Univ., Stanford, CA, 2012, <https://ctr.stanford.edu/proceedings-2012-summer-program>.
- [33] Sekhar, S., and Mansour, N. N., “Implicit LES of Turbulent, Separated Flow: Wall-Mounted Hump Configuration,” *53rd AIAA Aerospace Sciences Meeting*, AIAA Paper 2015-1966, 2015. doi:10.2514/6.2015-1966
- [34] Kawata, T., and Obi, S., “Velocity–Pressure Correlation Measurement Based on Planar PIV and Miniature Static Pressure Probes,” *Experiments in Fluids*, Vol. 55, No. 7, 2014, p. 1776. doi:10.1007/s00348-014-1776-7
- [35] Liu, X., and Thomas, F. O., “Measurement of the Turbulent Kinetic Energy Budget of a Planar Wake Flow in Pressure Gradients,” *Experiments in Fluids*, Vol. 37, No. 4, 2004, pp. 469–482. doi:10.1007/s00348-004-0813-3
- [36] Gutmark, E., and Wignanski, I., “The Planar Turbulent Jet,” *Journal of Fluid Mechanics*, Vol. 73, No. 3, 1976, pp. 465–495. doi:10.1017/S0022112076001468
- [37] Wignanski, I., and Fiedler, H., “Some Measurements in Self-Preserving Jet,” *Journal of Fluid Mechanics*, Vol. 38, No. 3, 1969, pp. 577–612. doi:10.1017/S0022112069000358
- [38] Kawata, T., Naka, Y., and Obi, S., “Simultaneous Measurement of Fluctuating Velocity and Pressure in the Near Wake of a Circular Cylinder,” *Experiments in Fluids*, Vol. 55, No. 5, 2014, p. 1731. doi:10.1007/s00348-014-1731-7
- [39] Terashima, O., Sakai, Y., and Nagata, K., “Simultaneous Measurement of Velocity and Pressure in a Plane Jet,” *Experiments in Fluids*, Vol. 53, No. 4, 2012, pp. 1149–1164. doi:10.1007/s00348-012-1351-z
- [40] Naka, Y., and Obi, S., “Velocity-Pressure Correlation Measurements in Complex Free Shear Flows,” *International Journal of Heat and Fluid Flow*, Vol. 30, No. 3, June 2009, pp. 411–420. doi:10.1016/j.ijheatfluidflow.2009.01.002
- [41] Naka, Y., Omori, T., Obi, S., and Masuda, S., “Simultaneous Measurement of Fluctuating Velocity and Pressure in a Turbulent Mixing Layer,” *International Journal of Heat and Fluid Flow*, Vol. 27, No. 4, 2006, pp. 737–746. doi:10.1016/j.ijheatfluidflow.2006.02.023
- [42] Hooper, J. D., and Musgrove, A. R., “Reynolds Stress, Mean Velocity, and Dynamic Static Pressure Measurement by a Four-Hole Pressure

- Probe," *Experimental Thermal and Fluid Science*, Vol. 15, No. 4, Nov. 1997, pp. 375–383.
doi:10.1016/S0894-1777(97)00005-8
- [43] Pope, S. B., *Turbulent Flows*, Cambridge Univ. Press, Cambridge, U.K., 2000.
- [44] Smith, A. M., and Cebeci, T., "Numerical Solution of the Turbulent-Boundary-Layer Equations," Douglas Aircraft Corp. Rept. DAC 33735, Aircraft Div., Long Beach CA, May 1967.
- [45] Baldwin, B., and Lomax, H., "Thin-Layer Approximation and Algebraic Model for Separated Turbulentflows," *16th Aerospace Sciences Meeting*, AIAA Paper 1978-257, Jan. 1978.
doi:10.2514/6.1978-257
- [46] Spalart, P., and Allmaras, S., "A One-Equation Turbulence Model for Aerodynamic Flows," *30th Aerospace Sciences Meeting and Exhibit*, AIAA Paper 1992-0439, Jan. 1992.
doi:10.2514/6.1992-439
- [47] Spalart, P. R., and Allmaras, S. R., "A One-Equation Turbulence Model for Aerodynamic Flows," *La Recherche Aerospaciale*, Vol. 1, No. 1, 1994, pp. 5–21.
- [48] Baldwin, B. S., and Barth, T. J., "A One-Equation Turbulence Transport Model for High Reynolds Number Wall-Bounded Flows," NASA TM 102847, 1990.
- [49] Jones, W. P., and Launder, B., "The Prediction of Laminarization with a Two-Equation Model of Turbulence," *International Journal of Heat and Mass Transfer*, Vol. 15, No. 2, 1972, pp. 301–314.
doi:10.1016/0017-9310(72)90076-2
- [50] Launder, B. E., and Sharma, B. I., "Application of the Energy-Dissipation Model of Turbulence to the Calculation of Flow Near a Spinning Disc," *Letters in Heat and Mass Transfer*, Vol. 1, No. 2, 1974, pp. 131–137.
doi:10.1016/0094-4548(74)90150-7
- [51] Wilcox, D. C., *Turbulence Modeling for CFD*, 3rd ed., DCW Industries, La Canada, CA, 2006.
- [52] Menter, F. R., "Two-Equation Eddy-Viscosity Turbulence Models for Engineering Applications," *AIAA Journal*, Vol. 32, No. 8, 1994, pp. 1598–1605.
doi:10.2514/3.12149
- [53] Girimaji, S. S., "Pressure–Strain Correlation Modeling of Complex Turbulent Flows," *Journal of Fluid Mechanics*, Vol. 422, Nov. 2000, pp. 91–123.
doi:10.1017/S0022112000001336
- [54] Speziale, C., Sarkar, S., and Gatski, T., "Modelling the Pressure–Strain Correlation of Turbulence: An Invariant Dynamical Systems Approach," *Journal of Fluid Mechanics*, Vol. 227, No. 1, 1991, pp. 245–272.
doi:10.1017/S0022112091000101
- [55] Chen, C.-J., and Jaw, S.-Y., *Fundamentals of Turbulence Modeling*, Taylor and Francis, Washington, D.C., 1998.
- [56] Lumley, J. L., "Computational Modeling of Turbulent Flows," *Advances in Applied Mechanics*, Vol. 18, 1978, pp. 123–176.
doi:10.1016/S0065-2156(08)70266-7
- [57] Fu, S., "Modeling of the Pressure–Velocity Correlation in Turbulence Diffusion," *Computers Fluids*, Vol. 22, Nos. 2–3, 1993, pp. 199–205.
doi:10.1016/0045-7930(93)90051-A
- [58] Schwarz, W. R., and Bradshaw, P., "Term-by-Term Tests of Stress-Transport Turbulence Models in a Three-Dimensional Boundary Layer," *Physics of Fluids*, Vol. 6, No. 2, 1994, pp. 986–998.
doi:10.1063/1.868330
- [59] Jeyapaul, E., and Rumsey, C., "Analysis of Highly-Resolved Simulations of 2-D Humps Toward Improvement of Second-Moment Closures," *51st AIAA Aerospace Sciences Meeting Including the New Horizons Forum and Aerospace Exposition*, AIAA Paper 2013-0684, Jan. 2013.
doi:10.2514/6.2013-684
- [60] Launder, B. E., Reece, G. J., and Rodi, W., "Progress in the Development of a Reynolds-Stress Turbulence Closure," *Journal of Fluid Mechanics*, Vol. 68, No. 3, 1975, pp. 537–566.
doi:10.1017/S0022112075001814
- [61] Naot, D., Shavit, A., and Wolfshtein, M., "Interactions Between Components of the Turbulent Velocity Correlation Tensor due to Pressure Fluctuations," *Israel Journal of Technology*, Vol. 8, No. 3, 1970, pp. 259–269.
- [62] Rogers, M. M., and Moin, P., "The Structure of the Vorticity Field in Homogeneous Turbulent Flows," *Journal of Fluid Mechanics*, Vol. 176, No. 1, 1987, pp. 33–66.
doi:10.1017/S0022112087000569
- [63] Demuren, A. O., Lele, S. K., and Durbin, P., "Role of Pressure Diffusion in Non-Homogeneous Shear Flows," *Proceedings of the Summer Program 1994*, Center for Turbulence Research, Stanford Univ., Stanford, CA, pp. 313–321.
- [64] Demuren, A. O., Rogers, M. M., Durbin, P., and Lele, S. K., "On Modeling Pressure Diffusion in Non-Homogeneous Shear Flows," *Proceedings of the 1996 Summer Program*, Center for Turbulence Research, Stanford Univ., Stanford, CA, 1996, pp. 63–72, <https://ctr.stanford.edu/proceedings-1996-summer-program>.
- [65] Rumsey, C. L., "Reynolds-Averaged Navier-Stokes Analysis of Zero Efflux Flow Control over a Hump Model," *Journal of Aircraft*, Vol. 44, No. 2, 2007, pp. 444–452.
doi:10.2514/1.23514
- [66] Gopalan, S., and Katz, J., "Flow Structure and Modelling Issues in the Closure Region of Attached Cavitation," *Physics of Fluids*, Vol. 12, No. 4, 2000, pp. 895–911.
doi:10.1063/1.870344
- [67] Gharib, M., "Response of the Cavity Shear Layer Oscillations to External Forcing," *AIAA Journal*, Vol. 25, No. 1, 1987, pp. 43–47.
doi:10.2514/3.9576
- [68] Gharib, M., and Roshko, A., "The Effect of Flow Oscillations on Cavity Drag," *Journal of Fluid Mechanics*, Vol. 177, No. 1, 1987, pp. 501–530.
doi:10.1017/S002211208700106X
- [69] Roth, G. I., "Developments in Particle Image Velocimetry (PIV) and their Application to the Measurement of the Flow Structure and Turbulence Within a Ship Bow Wave," Ph.D. Dissertation, Johns Hopkins Univ., Baltimore, MD, 1998.
- [70] Roth, G. I., and Katz, J., "Five Techniques for Increasing the Speed and Accuracy of PIV Interrogation," *Measurements Science of Technology*, Vol. 12, No. 3, 2001, pp. 238–245.
doi:10.1088/0957-0233/12/3/302
- [71] Bourassa, C., and Thomas, F. O., "An Experimental Investigation of a Highly Accelerated Turbulent Boundary Layer," *Journal of Fluid Mechanics*, Vol. 634, Sept. 2009, pp. 359–404.
doi:10.1017/S0022112009007289
- [72] Chang, K., Constantinescu, G., and Park, S.-O., "Analysis of the Flow and Mass Transfer Processes for the Incompressible Flow Past an Open Cavity with a Laminar and a Fully Turbulent Incoming Boundary Layer," *Journal of Fluid Mechanics*, Vol. 561, Aug. 2006, pp. 113–145.
doi:10.1017/S0022112006000735

L. Ukeiley
Associate Editor